Received 26 April 2016; | Revised 6 June 2016; | Accepted 6 June 2016

DOI: xxx/xxxx

RESEARCH ARTICLE

A Spatially Varying Robin Interface Condition for Fluid-Structure Coupled Simulations

Shunxiang Cao | Guangyao Wang | Kevin G. Wang

[1]Department of Aerospace and Ocean Engineering, Virginia Polytechnic Institute and State University, 460 Old Turner St. Blacksburg, 24061-0203, VA, USA

Correspondence
Kevin G. Wang, Aerospace and Ocean Engineering (MC0203) Randolph Hall 332-3 460 Old Turner St Blacksburg, VA 24061, USA. Email: kevinwgy@vt.edu

Present Address
Aerospace and Ocean Engineering (MC0203) Randolph Hall 332-3 460 Old Turner St Blacksburg, VA 24061, USA.

Summary

We present a spatially varying Robin interface condition for solving fluid-structure interaction problems involving incompressible fluid flows and non-uniform flexible structures. Recent studies have shown that for uniform structures with constant material and geometric properties, a one-parameter Robin interface condition can improve the stability and accuracy of partitioned numerical solution procedures. In this work, we generalize the constant parameter to a spatially varying function that depends on the structure's local material and geometric properties, without varying the exact solution of the coupled fluid-structure system. We present an algorithm to implement the Robin interface condition in an embedded boundary method for coupling a projection-based incompressible viscous flow solver with a nonlinear finite element structural solver. We demonstrate the numerical effects of the spatially varying Robin interface condition using two example problems: a simplified model problem featuring a non-uniform Euler-Bernoulli beam interacting with an inviscid flow, and a generalized Turek-Hron problem featuring a non-uniform, highly flexible beam interacting with a viscous laminar flow. Both cases show that a spatially varying Robin interface condition can clearly improve numerical accuracy (by up to 2 orders of magnitude in one instance) for the same computational cost. Using the second example problem, we also demonstrate and compare two models for determining the local value of the combination function in the Robin interface condition.

KEYWORDS:
fluid-structure interaction, partitioned procedure, Robin interface condition, embedded boundary method, incompressible flow, added mass effect

1 | INTRODUCTION

Extensive research has been devoted to developing partitioned procedures to couple computational fluid and structural dynamics solvers for simulating fluid-structure interaction (FSI) problems [1, 2, 3, 4, 5]. A common approach is to enforce the kinematic interface condition, i.e. the continuity of velocity across the fluid-structure interface, as a Dirichlet boundary condition in the fluid solver, and to enforce the dynamic interface condition, i.e. the continuity of stress, as a Neumann boundary condition in the structural solver. This type of Dirichlet-Neumann partitioned procedures have been used to simulate a broad range of FSI problems, including problems with large structural deformation, compressible flow, shock waves, and fluid-induced instabilities and failures (e.g., [6, 7, 8, 9, 10, 11])

Nonetheless, a well-known issue of Dirichlet-Neumann partitioned procedures is that for problems involving incompressible flow and strong added mass effect (e.g., heavy fluid, thin/slender structure), the scheme becomes unstable, regardless of the spatial and temporal discretization schemes used in the fluid and structural solvers. This issue, often referred to as the numerical (or artificial) added mass effect, has been formulated using simplified model problems [12, 13]. Specifically, Causin *et al.* [12] showed that a partitioned procedure becomes unconditionally unstable when the structure-to-fluid density ratio is below a threshold or the structure has a slender shape. Förster *et al.* [13] also investigated the stability criterion for several different temporal discretization schemes, and showed that they all become unconditionally unstable under strong added mass effect. A widely used approach to mitigate the numerical added mass effect is to perform subiterations between the fluid and structural solvers in the fashion of the Gauss-Seidel method [14, 15, 16, 17]. The drawback of this approach is obvious: it multiplies the computational cost by the number of subiterations. For example, Badia *et al.* [16] showed that to simulate a pressure wave propagating in a deformable pipe, a Dirichlet-Neumann partitioned procedure requires more than 100 subiterations per time step when the structure-to-fluid density ratio is equal to one.

Over the past decade, several research teams have investigated the use of Robin interface condition to mitigate the numerical added mass effect [18, 19, 5, 20, 21, 22, 23, 24, 25, 26, 27]. The basic idea is to substitute the kinematic interface condition by its linear combination with the dynamic interface condition. The resulting Robin-Neumann interface conditions are mathematically equivalent to the original Dirichlet-Neumann conditions, as long as the combination factor — denoted by α_f in this paper and several others — is nonzero. It has been shown that when α_f is carefully chosen, a Robin-Neumann partitioned procedure can eliminate the requirement of subiteration or reduce the number needed to achieve stability. For example, Badia *et al.* [18] proposed to design α_f based on simplified model equations (e.g., a linear piston), and have shown that for an example problem with a uniform membrane, a speed-up of up to one order of magnitude can be achieved. Nobile *et al.* [19, 5, 20] and Fernandez *et al.* [21, 22] have introduced the Robin interface condition to different types of partitioned procedures and fluid/structural governing equations, and demonstrated their performance in the context of blood flow - vessel wall interaction. To solve FSI problems involving complex geometry and large deformation, Cao *et al.* [23] have developed an algorithm to enforce the Robin interface condition using an embedded boundary method. We have also shown that when choosing the value of α_f, there is a trade-off: smaller values of α_f tend to improve numerical stability, while larger values give smaller numerical errors. Also, Li *et al.* [24] have introduced the Robin interface condition to the overset mesh framework. Basting *et al.* [25] have implemented it in an Arbitrary Lagrangian-Eulerian (ALE) framework with a variational mesh optimization algorithm. More generally, the idea of constructing a Robin interface condition to couple different physical domains has been applied to solve other multiphysics problems, such as fluid-structure-thermal interaction [28] and multiscale fracture mechanics [29].

Notably, previous studies on the use of Robin interface condition for fluid-structure coupling have focused on uniform structures with globally constant material and geometric properties. Examples include uniform beams and thin-walled tubes with constant thickness, density and elastic moduli. Moreover, previous studies have assumed that the Robin combination factor α_f is also a constant; while at the same time, several authors have suggested that in order to mitigate the numerical added mass effect, the value of α_f must be determined based on the material and geometry of the specific problem being solved (e.g., [18, 26, 23]). In this work, we generalize α_f to a spatially varying function, and investigate its numerical effects for FSI problems involving structures with spatially varying material properties. This study is motivated by three considerations. First, in real-world FSI problems, the structure of interest is often non-uniform, and may have complex geometry. For example, the density and the thickness of a thin-walled structure, either man-made or natural, often takes different values at different locations. Second, the previous findings mentioned above naturally suggest that if the geometric and material properties of the structure vary from one point to another, a globally constant α_f may not be optimal. It may be beneficial to generalize α_f to a variable function. Third, after generalizing α_f to a spatially varying function, the Robin-Neumann interface conditions remain mathematically equivalent to the original Dirichlet-Neumann conditions (as long as $\alpha_f \neq 0$). In other words, the generalization does not change the true solution of the coupled fluid-structure system.

More specifically, in this paper we address the following questions.

- Would a spatially varying combination function, $\alpha_f(\mathbf{X})$, outperform a constant α_f in terms of numerical accuracy and/or stability?
- If the answer to the above question is yes, how to design the function $\alpha_f(\mathbf{X})$ in order to achieve the improvement?

The remainder of this paper is organized as follows. In Section 2, we describe the context of this work by specifying the fluid and structural governing equations, constitutive models, and the Robin-Neumann interface conditions. Briefly speaking, we consider incompressible laminar fluid flows interacting with thin, elastic structures. Next, in Section 3 we investigate the

effects of spatially varying $\alpha_f(\mathbf{X})$ using a simplified model problem, in which the structure is an Euler-Bernoulli beam and the fluid domain is assumed to be fixed in time. Further, in Section 4, we consider a more realistic model problem, that is, a generalized Turek-Hron problem in which the flexible beam consists of multiple segments with different material properties. Using this example, we present the implementation of spatially varying $\alpha_f(\mathbf{X})$ in an embedded boundary framework, and discuss its numerical effects. In Section 5, we present and compare two model equations for determining the local value of the spatially varying combination function. Finally, we provide a few concluding remarks in Section 6.

2 | PHYSICAL MODEL

2.1 | Fluid and structural governing equations

We consider an incompressible viscous fluid flow interacting with a deformable structure, possibly with complex geometry and spatially varying material properties. The physical model couples the fluid governing equations defined in Ω_f and the structural governing equations defined in Ω_s (Figure 1). The fluid-structure interface, Σ, is thus defined by $\Sigma = \partial\Omega_f \cap \partial\Omega_s$. In this paper, we further assume that the fluid is Newtonian and the flow is laminar. Hence, its dynamics is governed by the following incompressible Navier-Stokes (N-S) equations.

$$\mathscr{F}(\mathbf{U}, P) = 0 := \begin{cases} \nabla \cdot \mathbf{U} = 0 & \text{in } \Omega_f, \quad (1a) \\ \dfrac{\partial \mathbf{U}}{\partial t} + \mathbf{U} \cdot \nabla \mathbf{U} - \nu \Delta \mathbf{U} + \dfrac{1}{\rho_f} \nabla P = 0 & \text{in } \Omega_f, \quad (1b) \end{cases}$$

where t denotes time, ρ_f is the fluid density, $\mathbf{U}$ is the fluid velocity vector, P is the fluid pressure and ν the kinematic viscosity. On the outer boundary of the fluid domain, different types of boundary conditions such as no-slip wall, inlet and outlet conditions may be applied, which can be written collectively as

$$\mathscr{B}(\mathbf{U}, P) = 0 \qquad \text{on } \partial\Omega_f \setminus \Sigma. \quad (2)$$

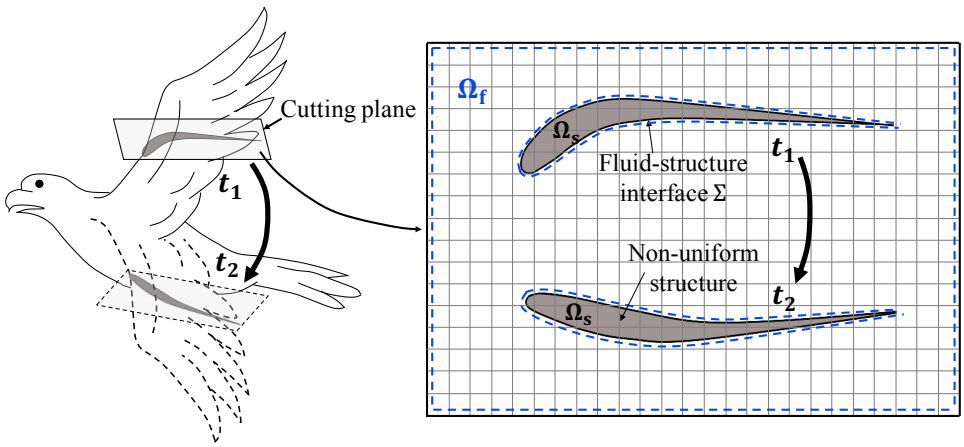

FIGURE 1 A fluid-structure interaction problem.

The structure is assumed to be elastic, and can have spatially varying material properties. To account for the possibility of large deformation, geometric nonlinearity is considered. Therefore, the dynamic equilibrium of the structure can be formulated as

$$\mathscr{S}(\mathbf{d}(\mathbf{X}, t)) = 0 := \rho_s(\mathbf{X}) \frac{\partial^2 \mathbf{d}(\mathbf{X}, t)}{\partial t^2} - \nabla \cdot \left(J^{-1} \mathbf{F} \mathbf{S} \mathbf{F}^T \right) - \rho_s(\mathbf{X}) \mathbf{b}(\mathbf{X}, t) = 0 \qquad \text{in } \Omega_s, \quad (3)$$

where $\mathbf{X}$ denotes the material coordinates, $\mathbf{d}$ denotes displacement, ρ_s denotes mass density, $\mathbf{S}$ is the second Piola-Kirchhoff (PK2) stress tensor, $\mathbf{F}$ is the deformation gradient, $J = \det \mathbf{F}$, and $\mathbf{b}$ denotes the body force per unit mass which is assumed to

be zero here. In this work, we apply the St. Venant-Kirchhoff constitutive model, given by

$$\mathbf{S} = \lambda_s tr(\mathbf{E})\mathbf{I} + 2\mu_s \mathbf{E}, \tag{4}$$

where $\mathbf{I}$ is the identity matrix, and $\mathbf{E} = \frac{1}{2}(\mathbf{F}^T\mathbf{F} - \mathbf{I})$. λ_s and μ_s are the Lamé coefficients.

The fluid-structure interface is assumed to be impermeable. Thus, the fluid and structural governing equations are coupled by a kinematic interface condition, i.e. the continuity of velocity (Eq. (5a)), and a dynamic interface condition, i.e. the continuity of stress (Eq. (5b))

$$\mathbf{U} = \frac{\partial \mathbf{d}}{\partial t} \qquad \text{on } \Sigma, \tag{5a}$$

$$\boldsymbol{\sigma}_f \mathbf{n} = \boldsymbol{\sigma}_s \mathbf{n} \qquad \text{on } \Sigma, \tag{5b}$$

where $\mathbf{n}$ denotes the unit normal pointing towards Ω_s. $\boldsymbol{\sigma}_f$ denotes the fluid stress tensor, given by $\boldsymbol{\sigma}_f = -P\mathbf{I} + 2\mu_f \mathbf{e}$, where $\mathbf{e}$ is the fluid strain rate tensor, and μ_f denotes the dynamic viscosity. $\boldsymbol{\sigma}_s$ denotes the Cauchy stress tensor of the structure, which can be related to PK2 stress by

$$\boldsymbol{\sigma}_s = J^{-1}\mathbf{F}\mathbf{S}\mathbf{F}^T.$$

2.2 | Spatially varying Robin interface condition

The Dirichlet interface condition, Eq. (5a), can be substituted by its linear combination with the Neumann interface condition, Eq. (5b), yielding a Robin interface condition. In this way, we obtain a pair of Robin-Neumann interface conditions[1], i.e.

$$\alpha_f(\mathbf{X})\frac{D\mathbf{U}}{Dt} + \boldsymbol{\sigma}_f \mathbf{n} = \alpha_f(\mathbf{X})\frac{\partial^2 \mathbf{d}}{\partial t^2} + \boldsymbol{\sigma}_s \mathbf{n} \qquad \text{on } \Sigma, \tag{6a}$$

$$\boldsymbol{\sigma}_f \mathbf{n} = \boldsymbol{\sigma}_s \mathbf{n} \qquad \text{on } \Sigma, \tag{6b}$$

where $D/Dt = \partial/\partial t + \mathbf{U} \cdot \nabla$, and α_f is the linear combination parameter. As mentioned in Section 1, previous studies have assumed α_f to be a constant parameter. Here, we generalize it to be a spatially varying function.

Equipped with this new pair of interface conditions, the fluid and structural sub-systems can be written as

$$\text{Fluid:} \begin{cases} \mathscr{F}(\mathbf{U}, P) = 0 & \text{in } \Omega_f \quad (7a) \\ \mathscr{B}(\mathbf{U}, P) = 0 & \text{on } \partial\Omega_f \setminus \Sigma \quad (7b) \\ \alpha_f(\mathbf{X})\dfrac{D\mathbf{U}}{Dt} + \boldsymbol{\sigma}_f \mathbf{n} = \alpha_f(\mathbf{X})\dfrac{\partial^2 \mathbf{d}}{\partial t^2} + \boldsymbol{\sigma}_s \mathbf{n} & \text{on } \Sigma \quad (7c) \end{cases}$$

$$\text{Structure:} \begin{cases} \mathscr{S}(\mathbf{d}) = 0 & \text{in } \Omega_s \quad (7d) \\ \boldsymbol{\sigma}_s \mathbf{n} = \boldsymbol{\sigma}_f \mathbf{n} & \text{on } \Sigma \quad (7e) \end{cases}$$

Next, we investigate the effect of the generalized, spatially varying α_f on the stability and accuracy of partitioned solution procedures, starting with a simplified model problem.

3 | A SIMPLIFIED MODEL PROBLEM

3.1 | Model setup

We consider a simplified model problem, in which a linear inviscid incompressible flow interacts with a *non-uniform* Euler-Bernoulli beam. Figure 2 presents a schematic drawing of the problem setup. The structure is a simply-supported Euler-Bernoulli beam, featuring lengthwise variation of density, $\rho_s(x)$ (Eq. (8a)). The other relevant material and geometric parameters — namely Young's modulus (E), and the width (b) and thickness (h) of the beam's cross section — are still assumed to be constant parameters. The fluid domain is a rectangular box underneath the beam, i.e. $\Omega_f = (0, L) \times (0, H)$. Given the small deformation of the beam, we assume that Ω_f does not change in time. Also, assuming an inviscid flow with a velocity field that has zero mean (in time) and small disturbance, the middle two terms in Eq. (1b) can be dropped, which leads to Eq. (8b). The left and right boundaries are assumed to be periodic (Eq. (8e)), while the bottom boundary is assumed to be a wall (Eq. (8d)).

[1] We note that in this work, as well as some previous studies (e.g., [24, 22]), the Robin condition combines the time derivative of Eq. (5a) with Eq. (5b), whereas in some other studies (e.g., [18]), the Robin condition directly combines Eq. (5a) with Eq. (5b).

$$\begin{cases} EI\dfrac{\partial^4 W}{\partial x^4} + \rho_s(x)bh\dfrac{\partial^2 W}{\partial t^2} = f(x,t) & \text{in } (0,T)\times\Omega_s \quad (8a)\\ \rho_f\dfrac{\partial \mathbf{U}}{\partial t} + \nabla P = 0 & \text{in } (0,T)\times\Omega_f \quad (8b)\\ \nabla\cdot\mathbf{U} = 0 & \text{in } (0,T)\times\Omega_f \quad (8c)\\ \mathbf{U}\cdot\mathbf{n} = 0 & \text{on } \Gamma_B \quad (8d)\\ \dfrac{\partial P}{\partial \mathbf{n}}\Big|_{\Gamma_L} = \dfrac{\partial P}{\partial \mathbf{n}}\Big|_{\Gamma_R}, P\Big|_{\Gamma_L} = P\Big|_{\Gamma_R}, & \quad (8e) \end{cases}$$

Here, W denotes the transverse displacement of the beam. ρ_f, U, and P denote fluid density, velocity, and pressure, respectively. Γ_L, Γ_R and Γ_B denote the left, right and bottom boundaries of Ω_f, respectively. f denotes the flow-induced force on the beam.

Since the beam is simply supported on both ends, we have

$$W(0,t) = W(L,t) = 0 \qquad \text{and} \qquad \frac{\partial^2 W(0,t)}{\partial x^2} = \frac{\partial^2 W(L,t)}{\partial x^2} = 0, \qquad \forall t > 0. \tag{9}$$

On the fluid-structure interface (Σ), the kinematic and dynamic interface conditions are given by

$$\mathbf{U}\cdot\mathbf{n} = \frac{\partial W}{\partial t} \qquad \text{and} \qquad f = Pb \qquad \text{on } \Sigma, \tag{10}$$

where $\mathbf{n}$ is the unit surface normal vector pointing towards the structure.

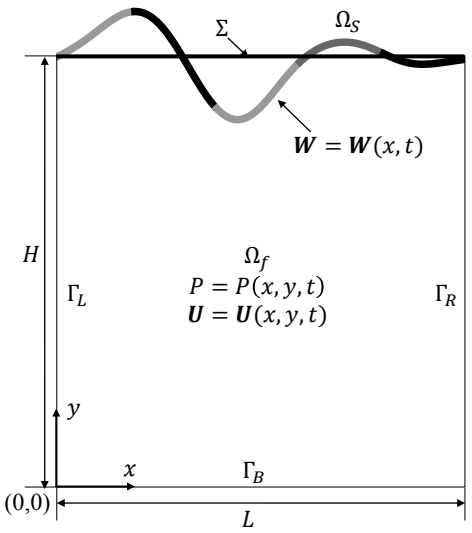

FIGURE 2 A simplified fluid-structure interaction model.

Combining Eqs. (8b) and (8c), we can eliminate the fluid velocity $\mathbf{U}$ from the system. Also, we combine the kinematic and dynamic interface conditions into a Robin interface condition, with a spatially varying combination factor $\alpha_f(x)$. After these manipulations, we obtain the following system of equations.

$$
\begin{cases}
EI\dfrac{\partial^4 W}{\partial x^4} + \rho_s(x)bh\dfrac{\partial^2 W}{\partial t^2} = f(x,t) & \text{in } (0,T)\times\Omega_s & \text{(11a)}\\
W = 0, \dfrac{\partial^2 W}{\partial x^2} = 0, & \text{at } x = 0 \text{ and } x = L & \text{(11b)}\\
\nabla^2 P = 0 & \text{in } (0,T)\times\Omega_f & \text{(11c)}\\
\dfrac{\partial P}{\partial y} = 0 & \text{on } \Sigma_B & \text{(11d)}\\
\dfrac{\partial P}{\partial y}\Big|_{\Gamma_L} = \dfrac{\partial P}{\partial y}\Big|_{\Gamma_R}, P\Big|_{\Gamma_L} = P\Big|_{\Gamma_R}, & & \text{(11e)}\\
\alpha_f(x)\dfrac{\partial P}{\partial y} + Pb = -\alpha_f(x)\rho_f\dfrac{\partial^2 W}{\partial t^2} + f & \text{on } \Sigma & \text{(11f)}\\
f = Pb. & \text{on } \Sigma & \text{(11g)}
\end{cases}
$$

We consider two representative cases in which the beam's density is defined to be a smoothed step function.

- Case 1 (Figure 3(a)): The beam's density, $\rho_s(x)$, features two distinct values with a smooth transition in between. It is defined by

$$\rho_s(x) = \frac{\rho_{s1} + e^{\gamma x - c}\rho_{s2}}{e^{\gamma x - c} + 1}, \tag{12}$$

  where $\rho_{s1} = 50\,\text{kg/m}^3$ and $\rho_{s2} = 4000\,\text{kg/m}^3$ define the two density values, i.e. the two "steps". c and γ are two parameters that control the location and width of the transition zone. Here, $c = 100$, $\gamma = 200\ \text{m}^{-1}$.

- Case 2 (Figure 3(b)): The beam's density, $\rho_s(x)$, features six steps. It is defined by

$$\rho_s(x) = \frac{\rho_s^{(k)} + e^{\gamma x - c^{(k)}}\rho_s^{(k+1)}}{e^{\gamma x - c^{(k)}} + 1}, \qquad \frac{(k-1)L}{5} \le x \le \frac{kL}{5}, \quad k = 1,2,3,4,5. \tag{13}$$

  In this case, $\rho_s^{(1)} = 4000\,\text{kg/m}^3$, $\rho_s^{(2)} = 2025\,\text{kg/m}^3$, $\rho_s^{(3)} = 50\,\text{kg/m}^3$, $\rho_s^{(4)} = 1366.67\,\text{kg/m}^3$, $\rho_s^{(5)} = 2683.33\,\text{kg/m}^3$, and $\rho_s^{(6)} = 4000\,\text{kg/m}^3$. Also, $c^{(1)} = 20$, $c^{(2)} = 60$, $c^{(3)} = 100$, $c^{(4)} = 140$, and $c^{(5)} = 180$, $\gamma = 200\ \text{m}^{-1}$.

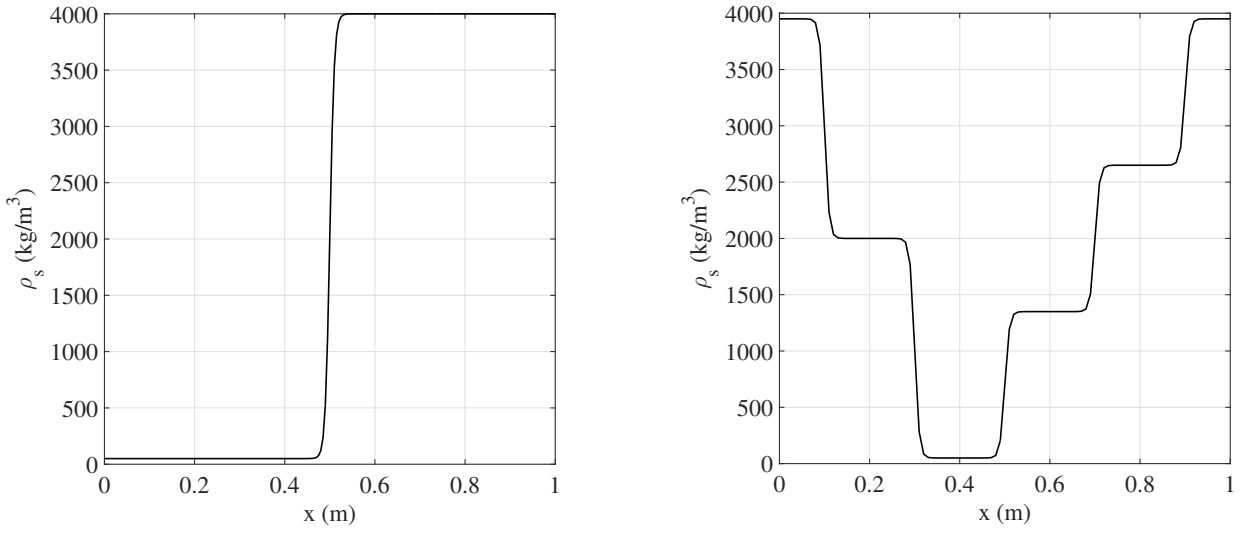

(a) Case 1 (b) Case 2

FIGURE 3 Two representative cases of non-uniform Euler-Bernoulli beam with spatially varying density.

In both cases, $E = 30$ GPa, $b = 0.01$ m, $h = 0.03$ m, $L = 1$ m, $H = 1$ m, and $\rho_f = 876$ kg/m^3. The initial displacement and acceleration of the beam are set to zero. The initial value of velocity is defined by

$$v(x, 0) = v_0 \sin\left(\frac{2n\pi x}{L}\right), \tag{14}$$

where $v_0 = 17.28$ m/s and $n = 3$. In addition, the initial (dynamic) pressure of the fluid is set to zero.

We solve this model problem using a standard partitioned procedure. The two-dimensional Laplace equation of the fluid sub-system is solved using the five-point finite difference scheme. The structural equation is semi-discretized using a standard Galerkin finite element method, then integrated in time using the Hilbert-Hughes-Taylor α (HHT-α) method. Additional details of the numerical solution procedure are provided in Appendix A.

Remarks:

- A simpler version of this problem, in which the beam has uniform density and α_f is a constant, has been solved both numerically and analytically (e.g., [30, 23]). Cao *et al.* [23] have derived the value of α_f that optimizes the trade-off between numerical stability and accuracy, i.e.

$$\alpha_{f,opt} = \frac{2}{\rho_f \left(\frac{1}{m_s} - \frac{1}{m_a}\right)}, \tag{15}$$

  where $m_s = \rho_s bh$ and $m_a = \dfrac{\rho_f b}{k \tanh(kH)}$ represent respectively the structural mass and the added mass of the fluid. The fact that $\alpha_{f,opt}$ depends on the structure's material and geometry (and how they compare with properties of the fluid flow) naturally suggests that for structures with spatially varying material properties or complex geometry, it may be advantageous to generalize α_f to a spatially varying function.

- In addition to the density of the beam, other parameters such as EI, b and h can also be generalized to spatially varying functions. We have tested some of these parameters. The results and findings obtained using a spatially varying density — to be presented in the next subsection — are found to be representative.

3.2 | Numerical analysis: Constant α_f versus $\alpha_f(x)$

3.2.1 | Case 1

Figures 4 and 5 show the converged numerical solution, which will be used as a reference for analyzing the effect of $\alpha_f(x)$ on accuracy. The accuracy of this reference solution has been verified by mesh convergence analysis and by comparison with the solution of a monolithic procedure, described briefly in Appendix A. Because of the spatial variation of the beam's density, the time history of mid-point deflection is not periodic (Figure 4), although the initial condition is a sine function. For the same reason, the magnitude of beam deflection and the fluid pressure are not symmetric with respect to the midline of the computational domain ($x = 0.5$ m).

Figure 6 presents the solutions obtained using the Robin-Neumann interface conditions with different constant values of α_f, in comparison with the reference solution. Both the fluid and the structural meshes have a resolution of 0.01 m. The time step size is set to be relatively large — specifically, 2×10^{-6} s — such that numerical errors can be easily observed and compared. Three different choices of α_f are presented in the figure, specifically, 3.0×10^{-5}, 4.0×10^{-5}, and 5.0×10^{-5} m^2 (for simplicity, we omit the unit m^2 for α_f in the rest of Section 3). Evidently, as α_f increases, the solution becomes more accurate. This is consistent with the result by Cao *et al.* [23] for a uniform beam with constant density. It is also notable that when α_f exceeds 5.0×10^{-5}, the numerical scheme becomes unconditionally unstable. For example, Figure 7 shows that with $\alpha_f = 5.1 \times 10^{-5}$, the solution blows up in less than 0.2 ms. Therefore, numerically we have found that for a specific pair of mesh resolution and time step size — which indicates a fixed computational cost — the most accurate solution that can be obtained using a constant α_f is given by $\alpha_f = 5.0 \times 10^{-5}$. The observed trade-off between accuracy and stability, when selecting a constant value for α_f, is also consistent with the finding of Cao *et al.* [23].

Next, we investigate the effects of a spatially varying $\alpha_f(x)$. Given that the beam density is a smoothed step function, we consider a simple model for $\alpha_f(x)$ that shares the same shape. Specifically, we define

$$\alpha_f(x) = \alpha_{f0} \frac{\rho_s(x)}{\rho_{s0}}, \tag{16}$$

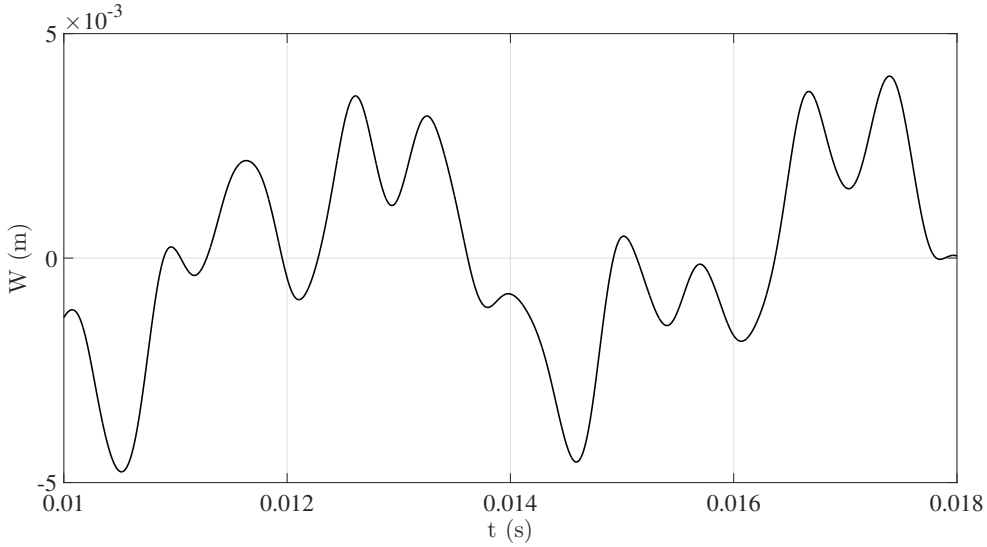

FIGURE 4 Converged solution of Case 1: Time history of beam displacement at the mid-point ($x = 0.50$ m).

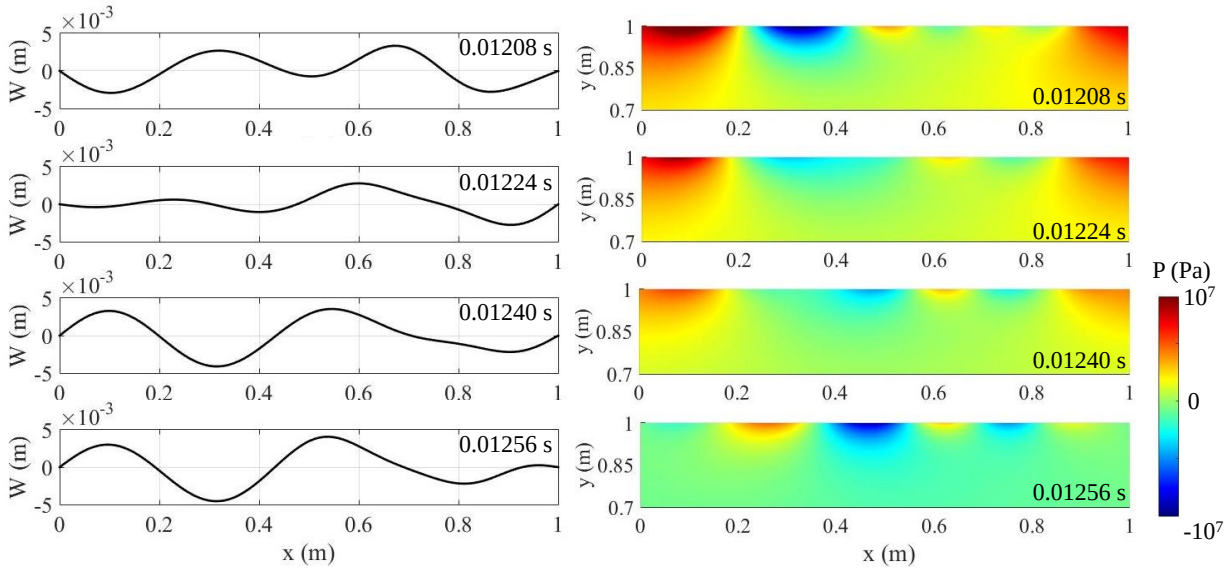

FIGURE 5 Snapshots of the converged solution of Case 1. Left: Beam deflection. Right: Fluid pressure. (Only the region above $y = 0.7$ m, where pressure varies significantly, is shown.)

where ρ_{s0} is the minimum value of density along the beam (50 kg/m^3 in this case), and α_{f0} is a constant value estimated based on ρ_{s0}. In this case, we set $\alpha_{f0} = 5 \times 10^{-5}$.

Figure 8 presents the relative error of the solution obtained using the above $\alpha_f(x)$, in comparison with the most accurate solution that can be obtained using a constant α_f, i.e. with $\alpha_f = 5.0 \times 10^{-5}$. Evidently, the use of a spatially varying function $\alpha_f(x)$ leads to a reduction of numerical error in both the fluid and the structural solutions. Specifically, the maximum relative error in beam deflection decreases by 21.09%, from 0.3930 to 0.3102, while in fluid pressure it decreases by 20.09%, from 0.3300 to 0.2637.

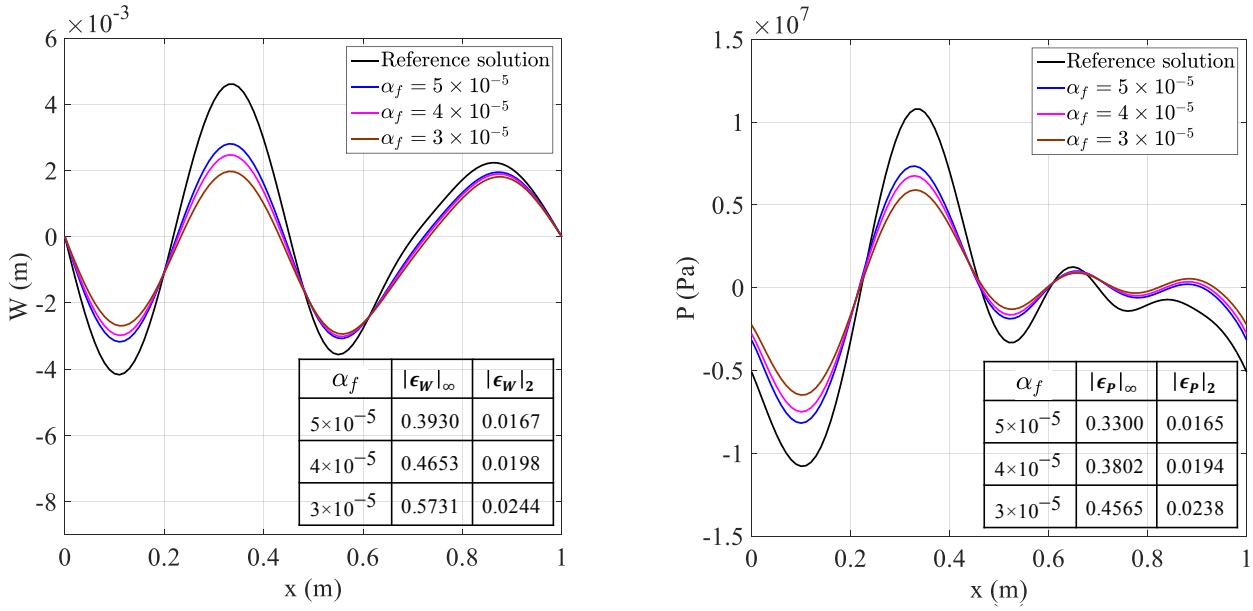

α_f	$\lvert\epsilon_W\rvert_\infty$	$\lvert\epsilon_W\rvert_2$
5×10^{-5}	0.3930	0.0167
4×10^{-5}	0.4653	0.0198
3×10^{-5}	0.5731	0.0244

(a) Beam displacement

α_f	$\lvert\epsilon_P\rvert_\infty$	$\lvert\epsilon_P\rvert_2$
5×10^{-5}	0.3300	0.0165
4×10^{-5}	0.3802	0.0194
3×10^{-5}	0.4565	0.0238

(b) Fluid pressure at the fluid-structure interface

FIGURE 6 Beam displacement at $t = 0.0015$ s obtained using different constant values of α_f, in comparison with the converged reference solution. ϵ_W and ϵ_P denote the relative error in beam displacement and the fluid pressure at interface, normalized using their maximum values.

3.2.2 | Case 2

For reference, Figure 9 shows a few snapshots of the converged fluid and structural solutions, which are independent of the choice of α_f.

When a constant α_f is applied, we find again, for fixed mesh resolution and time step size, the numerical solution becomes more accurate as the value of α_f increases, until α_f reaches a critical value, after which the solution blows up. For a 100-element structural mesh, a 100×100 fluid mesh, and a time step size of 2×10^{-6} s, this critical value is found to be 5.0×10^{-5}, same as in Case 1. This is likely because in both cases, the minimum value of the density function $\rho_s(x)$ are the same.

To investigate the effect of spatially varying $\alpha_f(x)$, we adopt the same model function introduced in Case 1, i.e. Eq. (16). Again, we set $\rho_{s0} = 50$ kg/m^3 and $\alpha_{f0} = 5.0 \times 10^{-5}$, based on the minimum value of the beam's density. Figure 10 compares the relative error in the structural and fluid solutions obtained using $\alpha_f(x)$ with the most accurate solution that can be obtained with a constant α_f, i.e., with $\alpha_f = 5.0 \times 10^{-5}$. Comparing with Figure 8 (Case 1), we find that the benefit of using a spatially varying $\alpha_f(x)$ is more significant in this case. Specifically, the maximum relative error in beam deflection and fluid pressure is reduced by 47.44% and 42.47%, respectively. Again, we note that this error reduction is achieved by exploiting the spatial variation of the structure's material property, with virtually no increase in computational cost.

4 | A MODIFIED TUREK-HRON MODEL PROBLEM

Based on the result obtained from the simplified model problem, we now move onto solving Eqs. (7) and investigating the effects of spatially varying Robin interface condition in a more realistic setting.

4.1 | Problem description

We consider a two-dimensional laminar incompressible channel flow interacting with a non-uniform, nonlinear beam mounted on the back of a fixed cylinder. Figure 11 shows the geometry of the problem. It is similar to the well-known Turek-Hron benchmark problem [31], except that the attached beam considered here consists of two segments, denoted by Γ_A and Γ_B, with

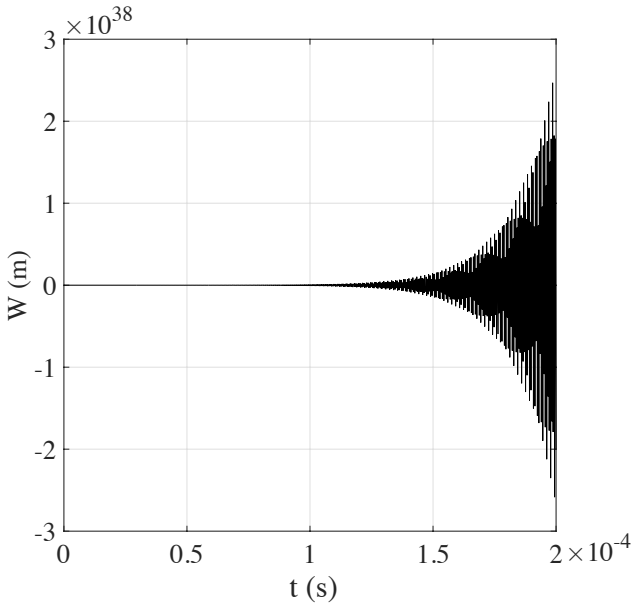

FIGURE 7 Time history of mid-point beam displacement obtained with $\alpha_f = 5.1 \times 10^{-5}$.

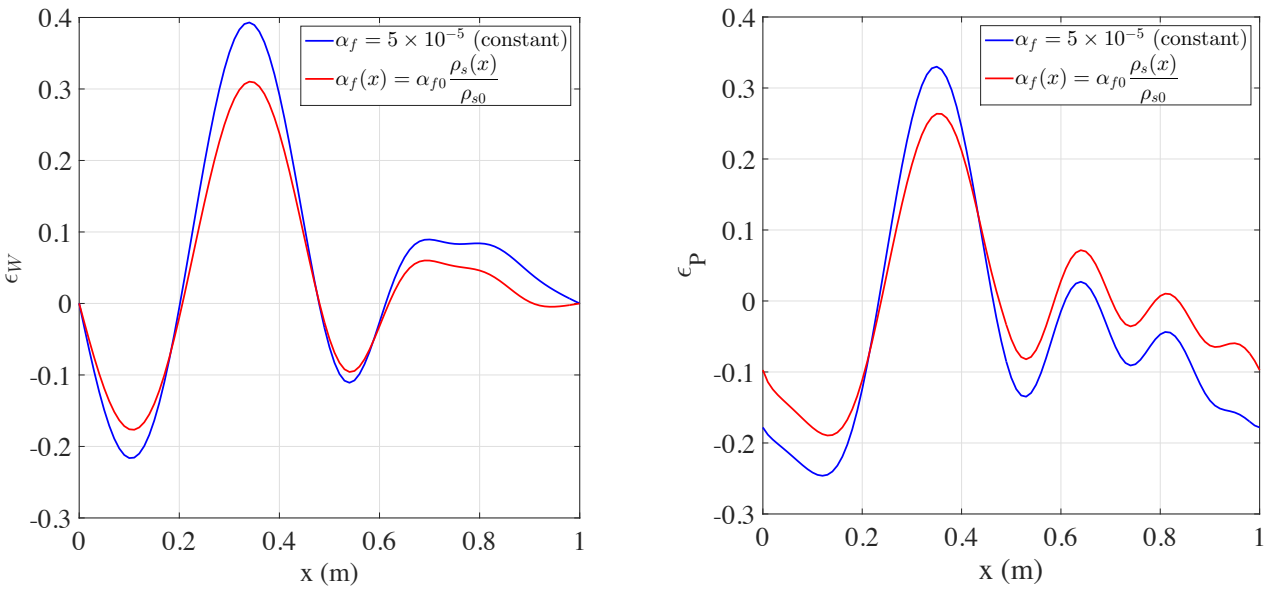

(a) Relative error in beam deflection

(b) Relative error in fluid pressure at interface (i.e. $y = 1$ m)

FIGURE 8 Comparison of constant α_f and a spatially varying function $\alpha_f(x)$ for Case 1.

significantly different mass densities. Specifically, the structure-to-fluid density ratio, ρ_s/ρ_f, is 0.3 in Γ_A and 10.0 in Γ_B. This indicates that segment Γ_A is subjected to stronger added mass effect. At the inflow boundary of the fluid domain, the following velocity profile is prescribed.

$$u(0, y, t) = 1.5\bar{U}\frac{y(H-y)}{(H/2)^2}, \qquad v(0, y, t) = 0, \tag{17}$$

where u and v denote the velocity components in the x and y directions. H is the height of the fluid domain and $\bar{U}$ is the average inflow velocity. At the channel outlet (i.e. the right boundary of the fluid domain), a "do nothing" boundary condition is applied.

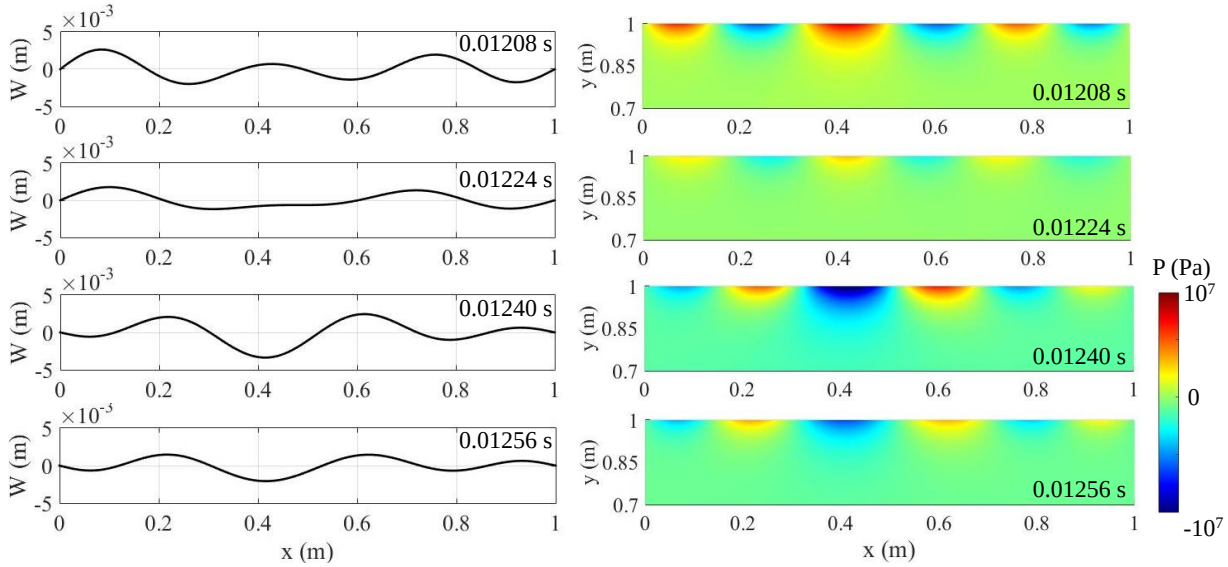

FIGURE 9 Snapshots of the converged solution of Case 2. Left: Beam deflection. Right: Fluid pressure. (Only the region above $y = 0.7$ m, where pressure varies significantly, is shown.)

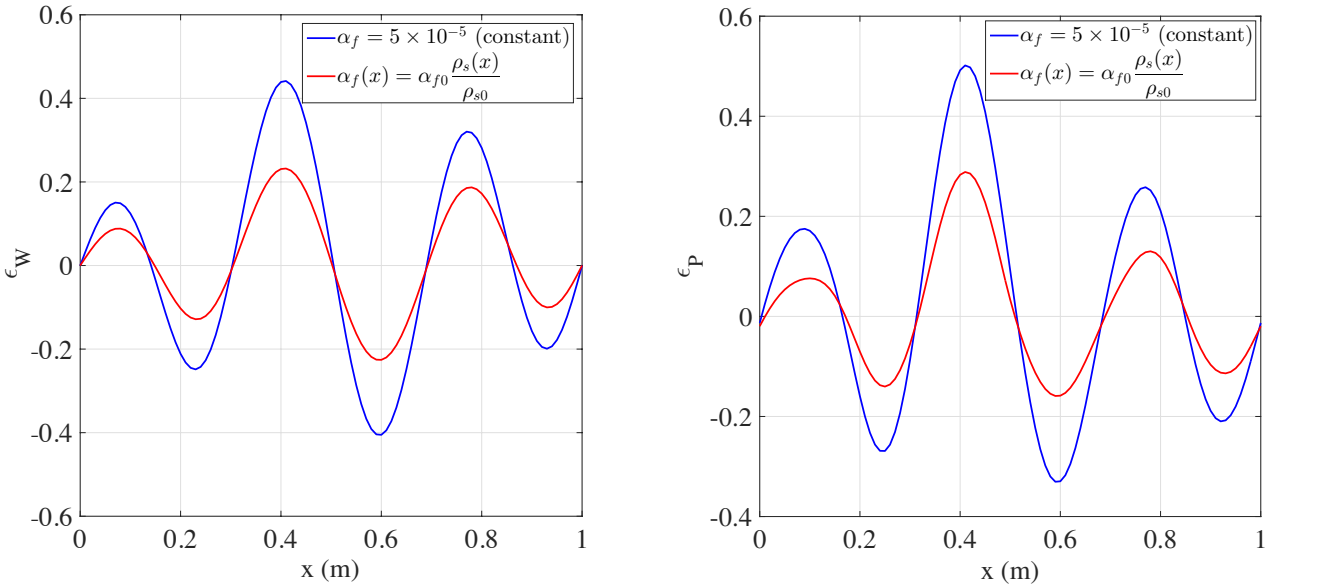

(a) Relative error in beam deflection

(b) Relative error in fluid pressure at the interface (i.e. $y = 1$ m)

FIGURE 10 Comparison of constant α_f and a spatially varying function $\alpha_f(x)$ for Case 2.

The no-slip boundary condition is enforced on the top and bottom walls. At the beginning of the simulation, the beam is at rest and straight as shown in the figure. Specific parameter values involved in this problem are given in Table 1.

4.2 | Numerical solution approach

We employ the fluid-structure coupled computational framework recently developed by Cao *et al.* [23]. The main components of this framework include a projection-based incompressible flow solver, a finite element structural dynamics solver, and an embedded boundary method to enforce the Robin transmission condition. The computational framework has been verified using

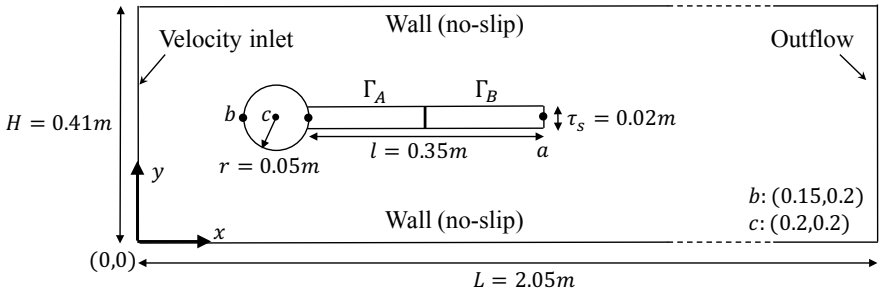

FIGURE 11 Geometry of the modified Turek-Hron benchmark problem.

	Segment Γ_A			Segment Γ_B			Fluid			
parameter	$\rho_s[kg/m^3]$	ν_s	$\mu_s[kg/(ms^2)]$	$\rho_s[kg/m^3]$	ν_s	$\mu_s[kg/(ms^2)]$	$\rho_f[kg/m^3]$	$\nu_f[m^2/s]$	$\bar{U}[m/s]$	Re
value	300	0.4	5.0×10^5	1.0×10^4	0.4	5.0×10^5	1×10^3	1×10^{-3}	1	100

TABLE 1 Parameters of the problem (ρ_s: density of the structure; ν_s: Poisson's ratio; μ_s: shear modulus; ρ_f: density of the fluid; ν_f: kinematic viscosity).

the original Turek-Hron benchmark problem with a uniform beam [31]. In this work, we extend the computational framework to enable the use of spatially varying Robin interface condition, i.e. Eq. (7c), and apply it to solve the modified Turek-Hron problem.

Specifically, the coupling between the fluid and structural sub-systems is based on an implicit coupling scheme which solves the two sub-systems iteratively at each time step. The following equations are solved to advance the system from time t^n to t^{n+1}.

$$\text{Fluid:} \begin{cases} \mathscr{F}(\mathbf{U}_{k+1}^{n+1}, P_{k+1}^{n+1}) = 0 & \text{in } \Omega_f \quad (18a) \\ \mathscr{B}(\mathbf{U}_{k+1}^{n+1}, P_{k+1}^{n+1}) = 0 & \text{on } \partial\Omega_f \setminus \Sigma \quad (18b) \\ \alpha_f(\mathbf{X}) \dfrac{D\mathbf{U}_{k+1}^{n+1}}{Dt} + \boldsymbol{\sigma}_{f,k+1}^{n+1}\mathbf{n} = \alpha_f(\mathbf{X}) \left(\dfrac{\partial^2 \mathbf{d}}{\partial t^2} \right)_k^{n^\star} + \boldsymbol{\sigma}_{s,k}^{n^\star}\mathbf{n} & \text{on } \Sigma \quad (18c) \end{cases}$$

$$\text{Structure:} \begin{cases} \mathscr{S}(\mathbf{d}_{k+1}^{n+1}) = 0 & \text{in } \Omega_s \quad (18d) \\ \boldsymbol{\sigma}_{s,k+1}^{n+1}\mathbf{n} = \boldsymbol{\sigma}_{f,k}^{n^\star}\mathbf{n} & \text{on } \Sigma \quad (18e) \end{cases}$$

where k is the index of subiteration. Also,

$$n^\star = \begin{cases} n, & \text{if } k = 0, \\ n+1, & \text{otherwise.} \end{cases}$$

At the fluid-structure interface (Σ), the latest solution information (i.e. fluid traction, structural acceleration and stress) are exchanged between the fluid and structural solvers, leading to a Gauss-Seidel type iteration.

To advance the fluid sub-system, the incompressible N-S equations are solved using a six-step, finite-difference projection method [32] on a cell-centered, collocated Cartesian grid. The spatially varying Robin interface condition, Eq. (18c), is enforced on the fluid-structure interface using an embedded boundary method. Specifically, we first discretize Eq. (18c) in time by

$$\alpha_f(\mathbf{X}) \left[\frac{\mathbf{U}_{k+1}^{n+1} - \mathbf{U}^n}{\Delta t} + (\mathbf{U} \cdot \nabla \mathbf{U})_k^{n^\star} \right] + \boldsymbol{\sigma}_{f,k+1}^{n+1}\mathbf{n} = \alpha_f(\mathbf{X}) \left(\frac{\partial^2 \mathbf{d}}{\partial t^2} \right)_k^{n^\star} + \boldsymbol{\sigma}_{s,k}^{n^\star}\mathbf{n} \qquad \text{on } \Sigma, \tag{19}$$

where the structural acceleration $\left(\partial^2 \mathbf{d}/\partial t^2\right)$ is computed by the structural solver, then transferred to the fluid solver. Then, we apply an operator splitting method to split Eq. (19) in the same fashion as the projection method in the incompressible flow

solver. This leads to

$$\begin{cases} \mathbf{U}_{k+1}^{*,n+1} = \mathbf{U}^n + \dfrac{\Delta t}{\alpha_f(\mathbf{X})} \left\{ -\boldsymbol{\sigma}_{f,k+1}^{*,n+1}\mathbf{n} + \alpha_f(\mathbf{X}) \left(\dfrac{\partial^2 \mathbf{d}}{\partial t^2} \right)_k^{n^\bullet} + \boldsymbol{\sigma}_{s,k}^{n^\bullet}\mathbf{n} - \alpha_f(\mathbf{X}) \left(\mathbf{U} \cdot \nabla \mathbf{U} \right)_k^{n^\bullet} \right\} & \text{on } \Sigma, \quad (20a) \\ -\dfrac{\alpha_f(\mathbf{X})}{\Delta t} \left(\dfrac{\partial \phi}{\partial \mathbf{n}} \right)_{k+1}^{n+1} + \hat{\boldsymbol{\sigma}}_{f,k+1}^{n+1}\mathbf{n} \cdot \mathbf{n} = 0 & \text{on } \Sigma. \quad (20b) \end{cases}$$

Here, $\mathbf{U}^*$ denotes the intermediate velocity, i.e. the solution of the fluid momentum equation. ϕ is an auxiliary variable in projection step. $\boldsymbol{\sigma}^*$ and $\hat{\boldsymbol{\sigma}}$ denote the two components of the decomposed fluid stress tensor. Eq. (20a) is enforced on the embedded interface as the boundary condition for $\mathbf{U}^*$, using a ghost-cell method [33]. Eq. (20b) is enforced on the embedded interface as the boundary condition for Poisson's equation in projection step, using an asymmetric finite difference scheme [34, 35]. The algorithm for solving the fluid sub-system is summarized in Algorithm 1. For additional details of the projection method and the embedded Robin boundary method, we refer the reader to [23].

Algorithm 1 Algorithm for the fluid sub-system

1: Solve the momentum equation for intermediate velocity $\mathbf{U}_{k+1}^{*,n+1}$:

$$(\mathbf{I} - \eta_2 \nu \mathbf{L})(\mathbf{I} - \eta_1 \nu \mathbf{L})\mathbf{U}_{k+1}^{*,n+1} = (\mathbf{I} + \eta_3 \nu \mathbf{L})\mathbf{U}^n - \Delta t(\mathbf{I} + \eta_4 \nu \mathbf{L}) \left(\mathbf{N}^{n+\frac{1}{2}} + \frac{1}{\rho_f} \mathbf{G} P^{n-\frac{1}{2}} \right) \quad \text{in } \Omega_f, \quad (21)$$

$$\mathbf{U}_{k+1}^{*,n+1} = \mathbf{U}^n + \frac{\Delta t}{\alpha_f(\mathbf{X})} \left\{ -\boldsymbol{\sigma}_{f,k+1}^{*,n+1}\mathbf{n} + \alpha_f(\mathbf{X}) \left(\frac{\partial^2 \mathbf{d}}{\partial t^2} \right)_k^{n^\bullet} + \boldsymbol{\sigma}_{s,k}^{n^\bullet}\mathbf{n} - \alpha_f(\mathbf{X}) \left(\mathbf{U} \cdot \nabla \mathbf{U} \right)_k^{n^\bullet} \right\} \quad \text{on } \Sigma. \quad (22)$$

where $\mathbf{L}$ and $\mathbf{G}$ denotes the discrete Laplace operator and the discrete gradient operator, $\mathbf{I}$ is the identity operator, and $\mathbf{N}^{n+\frac{1}{2}}$ represents an approximation of the nonlinear advection term.

2: Project $\mathbf{U}_{k+1}^{*,n+1}$ onto a space that satisfies the divergence-free constraint:

$$\mathbf{L}(\phi_{k+1}^{n+1}) = \mathbf{D}\mathbf{U}_{k+1}^{*,n+1} \quad \text{in } \Omega_f, \quad (23)$$

$$-\frac{\alpha_f(\mathbf{X})}{\Delta t} \left(\frac{\partial \phi}{\partial \mathbf{n}} \right)_{k+1}^{n+1} + \hat{\boldsymbol{\sigma}}_{f,k+1}^{n+1}\mathbf{n} \cdot \mathbf{n} = 0 \quad \text{on } \Sigma. \quad (24)$$

where D denotes the discrete divergence operator.

3: Update velocity at time t^{n+1}:

$$\mathbf{U}_{k+1}^{n+1} = \mathbf{U}_{k+1}^{*,n+1} - \mathbf{G}\phi_{k+1}^{n+1}. \quad (25)$$

4: Solve the momentum equation again without the pressure gradient term for intermediate velocity $\widetilde{\mathbf{U}}_{k+1}^{*,n+1}$:

$$(\mathbf{I} - \eta_2 \nu \mathbf{L})(\mathbf{I} - \eta_1 \nu \mathbf{L})\widetilde{\mathbf{U}}_{k+1}^{*,n+1} = (\mathbf{I} + \eta_3 \nu \mathbf{L})\mathbf{U}^n - \Delta t(\mathbf{I} + \eta_4 \nu \mathbf{L})\mathbf{N}^{n+\frac{1}{2}} \quad \text{in } \Omega_f, \quad (26)$$

$$\widetilde{\mathbf{U}}_{k+1}^{*,n+1} = \mathbf{U}^n + \frac{\Delta t}{\alpha_f(\mathbf{X})} \left\{ -\boldsymbol{\sigma}_{f,k+1}^{*,n+1}\mathbf{n} + \alpha_f(\mathbf{X}) \left(\frac{\partial^2 \mathbf{d}}{\partial t^2} \right)_k^{n^\bullet} + \boldsymbol{\sigma}_{s,k}^{n^\bullet}\mathbf{n} - \alpha_f(\mathbf{X}) \left(\mathbf{U} \cdot \nabla \mathbf{U} \right)_k^{n^\bullet} \right\} \quad \text{on } \Sigma. \quad (27)$$

5: Project $\widetilde{\mathbf{U}}_{k+1}^{*,n+1}$ onto a space that satisfies the divergence-free constraint:

$$\mathbf{L}(\widetilde{\phi}_{k+1}^{n+1}) = \mathbf{D}\widetilde{\mathbf{U}}_{k+1}^{*,n+1} \quad \text{in } \Omega_f, \quad (28)$$

$$-\frac{\alpha_f(\mathbf{X})}{\Delta t} \left(\frac{\partial \widetilde{\phi}}{\partial \mathbf{n}} \right)_{k+1}^{n+1} + \hat{\boldsymbol{\sigma}}_{f,k+1}^{n+1}\mathbf{n} \cdot \mathbf{n} = 0 \quad \text{on } \Sigma. \quad (29)$$

6: Update fluid pressure at time t^{n+1}:

$$P_{k+1}^{n+\frac{1}{2}} = \frac{\rho_f}{\Delta t}(\mathbf{I} + \eta_4 \nu \mathbf{L})^{-1}(\mathbf{I} - \eta_2 \nu \mathbf{L})(\mathbf{I} - \eta_1 \nu \mathbf{L})\widetilde{\phi}_{k+1}^{n+1} \quad \text{in } \Omega_f. \quad (30)$$

Again, we emphasize that in Eq. (20), α_f is a spatially varying function. Nonetheless, as long as a closed-form formulation is available, the computational overhead caused by this generalization is negligible.

For the structural sub-system, we consider a geometrically nonlinear beam in 2-D, and semi-discretize the governing equation (Eq. (18d)) using the continuum-based beam element [36]. Specifically, the beam is modeled as a set of adjoining quadrilateral beam elements, which relies on two assumptions: (1) the fibers are straight and inextensible; and (2) the beam is in a state of plane stress. The equation of motion for each element can be written as

$$\mathbf{M}_e\ddot{\mathbf{u}}_e^m + \mathbf{T}_e^T\mathbf{M}_e^s\dot{\mathbf{T}}_e\dot{\mathbf{u}}_e^m + \mathbf{f}^{int} = \mathbf{f}^{ext}, \tag{31}$$

where $\mathbf{u}_e^m$ denotes the motion of the master nodes, M_e is the mass matrix, $\mathbf{T}_e$ is the transformation matrix, $\mathbf{M}_e^s$ is the mass matrix for the quadrilaterial continuum element. $\mathbf{f}^{int}$ and $\mathbf{f}^{ext}$ denote the internal and external nodal forces, respectively. The time integration of Eq. (31) is done using the Newmark-β algorithm. To avoid redundancy, we refer the reader to Main [37] for additional details of the structural solver.

4.3 | Result

Figures 12 and 13 present the converged numerical solution, specifically, the fluid vorticity, pressure and the beam 's deformation at four time instants during one period of beam vibration. It is clear that vortex shedding and vortex-induced structural vibration are the dominating features of this problem. In addition, Figure 14(a) presents the time history of the vertical displacement (δy) at the beam tip (i.e. point a in Figure 11). After the beam reaches a periodic steady state, the tip displacement varies within $\delta y \in [-0.089, 0.0915]$ m, with a period of 0.48 seconds. It is interesting to compare the solution of the current problem with that of the original Turek-Hron benchmark problem (test case FSI-2), as they only differ in the beam's density within Γ_A. Figure 14(b) compares the vertical displacement at the beam tip. Even though the density within Γ_A is more than one order of magnitude smaller in the current problem, the vibration frequency and amplitude only change slightly. This is because the other properties of the beam (e.g., elastic moduli, thickness) and the Reynolds number of the flow remain unchanged. And the Reynolds number is known as the key factor of the vortex shedding of the cylinder that drives the beam's vibration.

To obtain a reference solution for error analysis, a mesh convergence analysis has been conducted using Cartesian fluid meshes with resolution of 250×50, 500×100, and 1000×200. The solutions obtained using the last two meshes differ by less than 2%, in terms of the maximum vertical displacement at the beam tip. A temporal convergence analysis has also been conducted for 3.0×10^{-4} s $\leq \Delta t \leq 1.2 \times 10^{-3}$ s, using the 500×100 fluid mesh and 80 beam elements (Figure 15). The solutions given by $\Delta t = 6.0 \times 10^{-4}$ s and $\Delta t = 3.0 \times 10^{-4}$ s differ by 2.1%, also in terms of the maximum vertical displacement at the beam tip. The results presented in Figures 12, 13, and 14 are computed using the 1000×200 fluid mesh, a structural mesh with 160 elements, and a time step size of 4.1×10^{-4} s. Also, six fluid-structure subiterations are performed at each time step.

4.4 | Constant α_f versus $\alpha_f(\mathbf{X})$

We design two groups of numerical experiments. In the first group, a constant α_f is specified over the entire beam structure. In the second group, a spatially varying $\alpha_f(\mathbf{X})$ is applied. Specifically, because the beam has two segments, and the density remains constant within each segment, we define $\alpha_f(\mathbf{X})$ to be a piecewise constant function, given by

$$\alpha_f(\mathbf{X}) = \alpha_{f,A}\mathbb{1}_{\Gamma_A} + \alpha_{f,B}\mathbb{1}_{\Gamma_B} = \begin{cases} \alpha_{f,A}, & \text{in } \Gamma_A, \\ \alpha_{f,B}, & \text{in } \Gamma_B. \end{cases} \tag{32}$$

All the computations are carried out using a 500×100 fluid mesh, a structural mesh with 80 elements, a time step of 8.2×10^{-4}s, and a fixed number of subiterations (3 per time step). Hence, the results from both groups are obtained with the same computational cost.

In the first group, we vary the value of α_f over a broad range, from 2.0 to 1.0×10^6 kg/m^2, and determine the threshold value for achieving numerical stability. For simplicity, we omit the unit kg/m^2 for α_f in the rest of the paper. The result shows that the solution is stable if and only if $\alpha_f \leq 4.25$. This is demonstrated by Figure 16 in which the fluid pressure fields obtained with $\alpha_f = 4.25$ and $\alpha_f = 4.5$ are compared. It is clear that for $\alpha_f = 4.5$ — a value slightly above the limit — the pressure field oscillates, and as time increases, both the structural and the fluid solutions blow up. Notably, the numerical instability initiates around segment Γ_A of the beam, where the structure-to-fluid density ratio is small. This indicates that if a constant α_f is used for

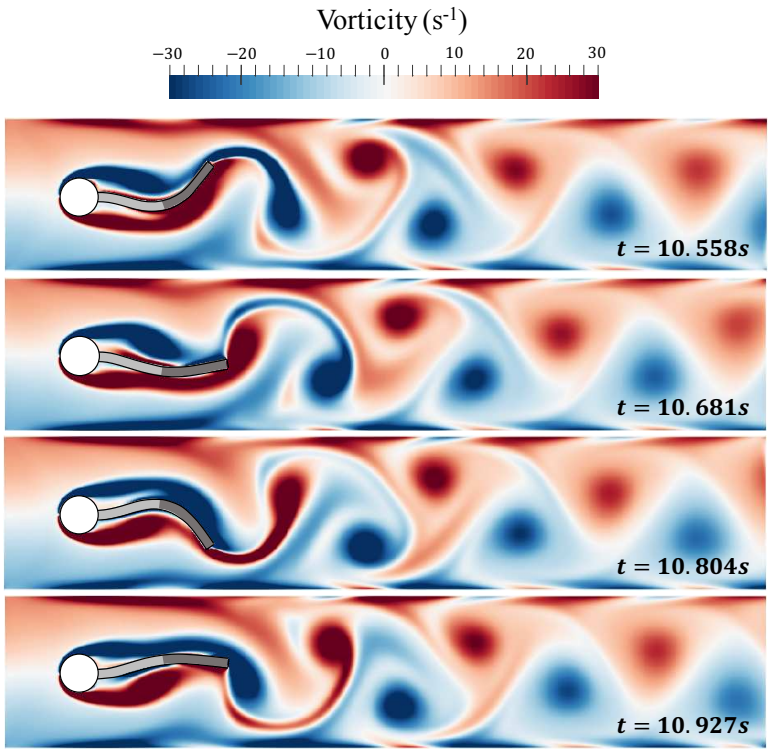

FIGURE 12 Vorticity at four time instances during one period of beam vibration.

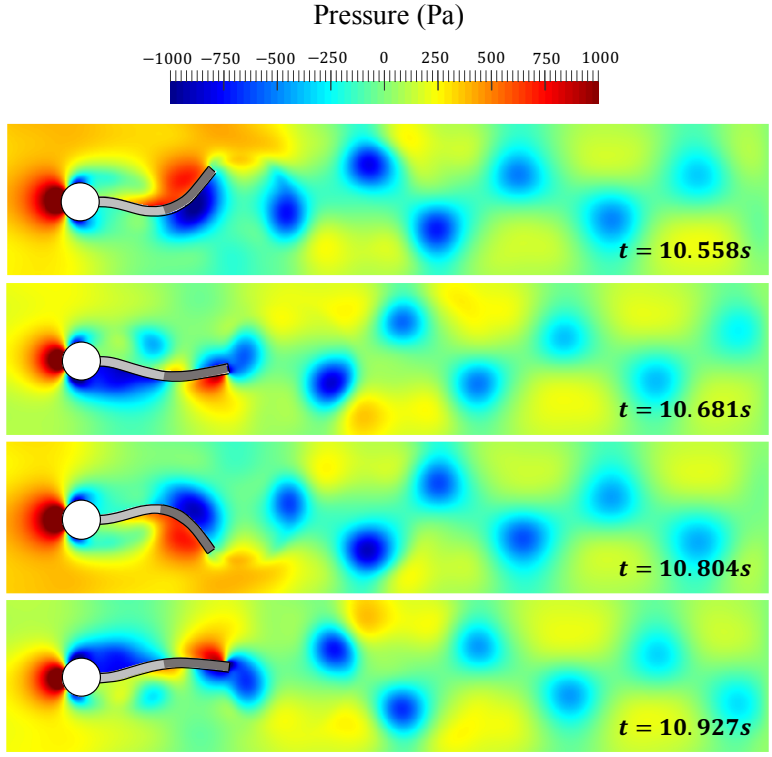

FIGURE 13 Fluid pressure at four time instances during one period of beam vibration.

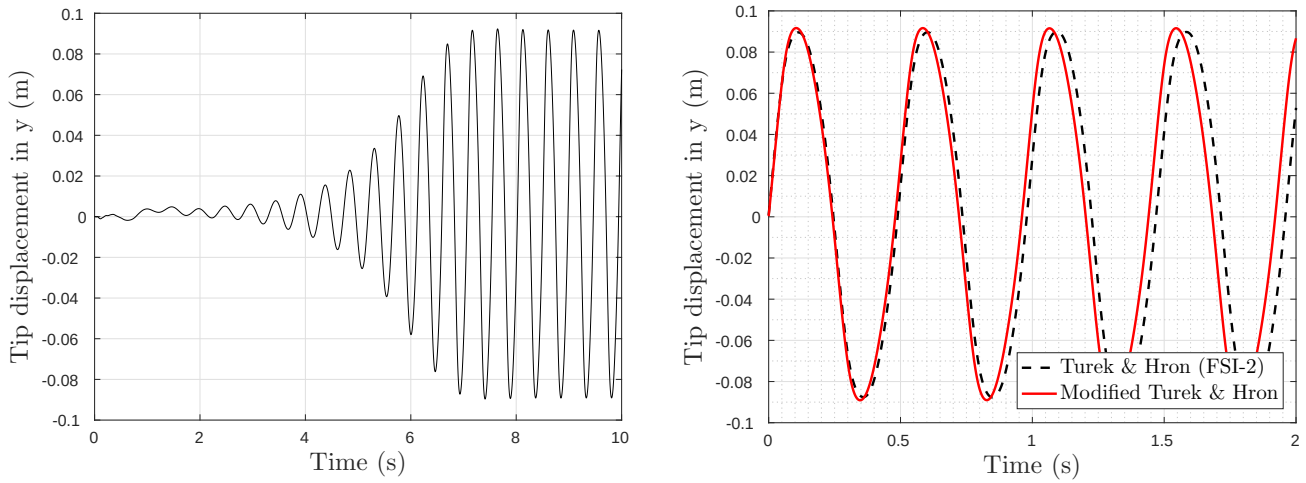

FIGURE 14 (a) Time history of beam tip displacement in y direction; (b) Comparison with the original Turek-Hron benchmark problem (test case FSI-2) [31]. In Subfigure (b), time is synchronized for the easy of comparison. The synchronized time instance 0 corresponds to 7.591 s in the original Turek-Hron problem, and 7.543 s in the modified one.

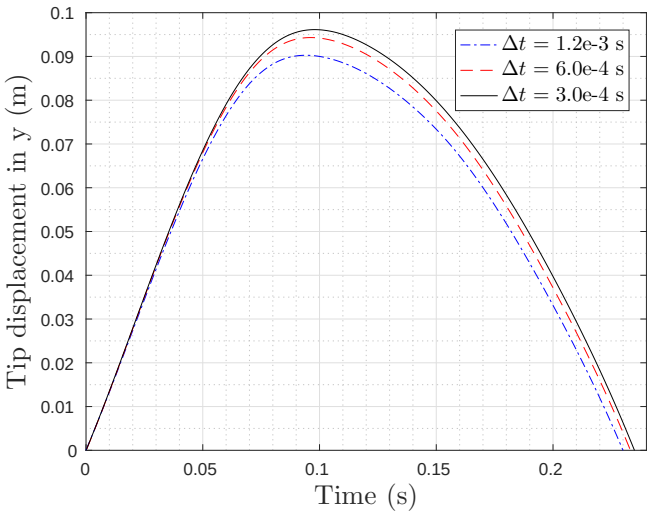

FIGURE 15 Temporal convergence result

solving FSI problems with a non-uniform structure, the largest value of α_f that can be used (to achieve better accuracy without losing stability) is likely determined by the region with strongest added mass effect.

To examine the effect of constant α_f on numerical accuracy, Figure 17 presents the solutions obtained with three values, $\alpha_f = 4.25$, 4.0, and 3.0, in comparison with the converged reference solution. It is clear that the solution becomes less accurate as α_f is reduced. The trade-off between stability and accuracy is consistent with the finding shown by Cao *et al.* [23] for the original Turek-Hron problem. Notably, the solution obtained with $\alpha_f = 4.25$ represents the most accurate solution that can be obtained using a constant α_f for the chosen meshes, time step size, and number of subiterations (i.e. a fixed computational cost).

In the second group of experiments, we consider the use of a piecewise constant $\alpha_f(\mathbf{X})$, with $\alpha_{f,A}$ fixed to 3.0, and $\alpha_{f,B}$ varied over a broad range, from 3.0 to 1.0×10^6. For example, Figure 17 shows the solutions of two trials, $\alpha_{f,B} = 100.0$ and 1.0×10^6, in comparison with the reference solution. In both cases, the predicted maximum displacement at beam tip differs from the

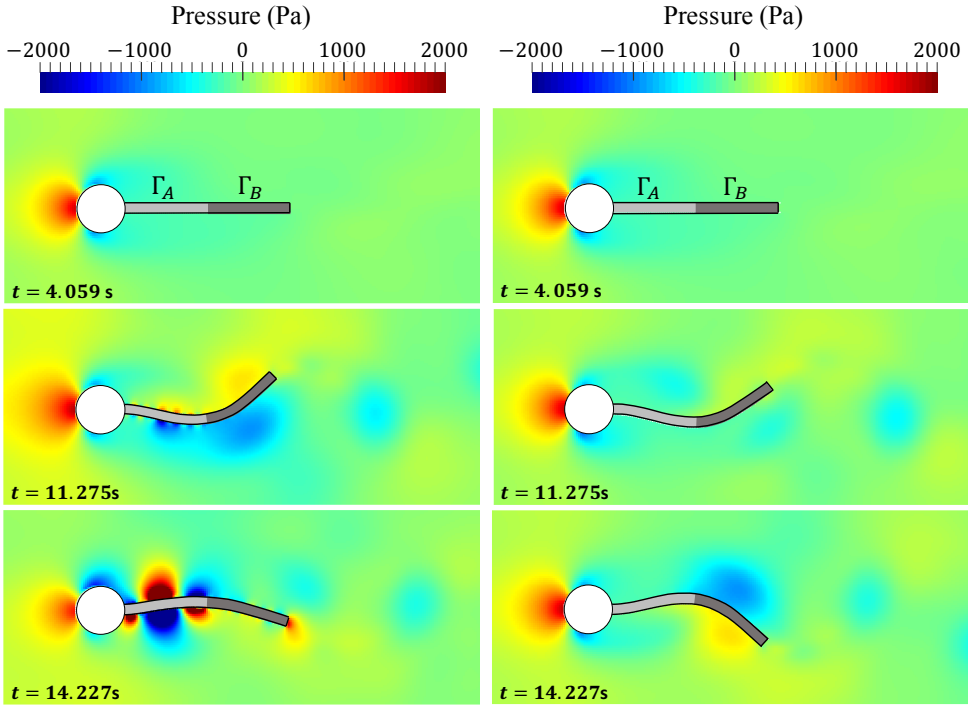

(a) $\alpha_f = 4.5$, unstable (b) $\alpha_f = 4.25$, stable

FIGURE 16 Comparison of fluid pressure obtained using two constant values of α_f across the stability limit.

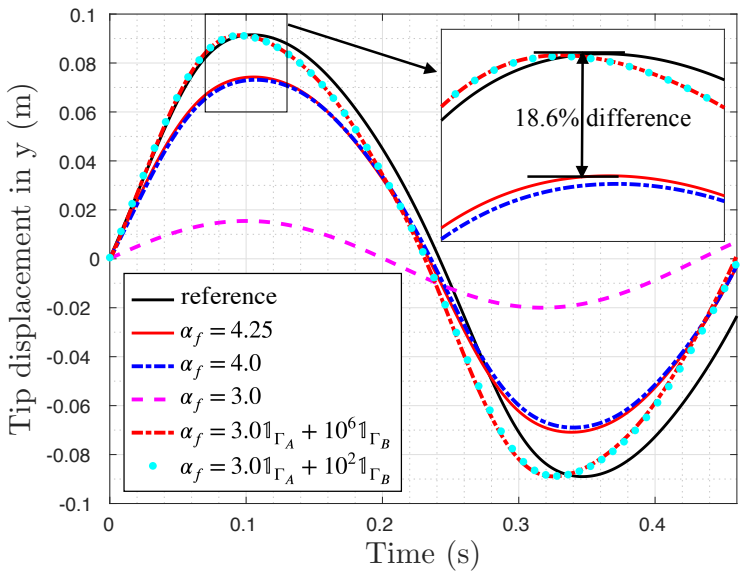

FIGURE 17 Comparison of beam tip displacement obtained with different constant values of α_f and spatially varying $\alpha_f(X)$.

reference solution by less than 1%. More importantly, for both cases, the solutions are more accurate than the most accurate solution that can be obtained using a constant α_f.

Table 2 summarizes the relative error in maximum vertical tip displacement (ϵ_d) obtained using different constant values of α_f and spatially varying $\alpha_f(\mathbf{X})$. Comparing the trials in each group — that is, trials 1 through 4 and 5 through 8 — we find

that for both constant and spatially varying α_f, numerical accuracy improves as α_f increases, until exceeding the stability limit. Comparing trial 1 with trial 7, it is evident that increasing the value of α_f in Γ_B from 3.0 to 100.0 leads to dramatic improvement in accuracy. In this case, ϵ_d decreases from 82.9% to 0.2%, by a factor of over 415. Also, comparing trial 3 with trial 7, we see that for this benchmark problem, a spatially varying α_f outperforms the optimal constant value of α_f by a factor of 93, without increasing the computational cost.

	Constant α_f				Spatially varying α_f			
Trial no.	1	2	3	4	5	6	7	8
α_f	3.0	4.0	4.25	4.5	$3.0\mathbb{1}_{\Gamma_A} + 5.0\mathbb{1}_{\Gamma_B}$	$3.0\mathbb{1}_{\Gamma_A} + 10.0\mathbb{1}_{\Gamma_B}$	$3.0\mathbb{1}_{\Gamma_A} + 10^2\mathbb{1}_{\Gamma_B}$	$3.0\mathbb{1}_{\Gamma_A} + 10^6\mathbb{1}_{\Gamma_B}$
ϵ_d	82.9%	19.7%	18.6%	N/A*	20.0%	10%	0.2%	0.2%

* unstable.

TABLE 2 Comparison of constant values of α_f with spatially varying α_f: Numerical error in maximum vertical tip displacement (ϵ_d).

5 | MODELS FOR THE SPATIALLY VARYING COMBINATION FACTOR

5.1 | Two models

We present two models for determining the local value of $\alpha_f(\mathbf{X})$ in the spatially varying Robin interface condition (Eq. (7c)). Based on the findings shown in the previous sections, we take two factors into account in the design of such models. First, the model should account for the trade-off between stability and accuracy, i.e., one would prefer to increase the value of α_f, but must avoid "falling off the cliff", that is, exceeding the stability limit. Second, a point on the structure subjected to stronger added mass effect requires a smaller value of α_f at that point to maintain stability.

Previous studies have indicated that α_f should depend on the density of the structure and — for thin-walled and slender structures — its thickness (e.g., [18, 23]). Therefore, we first build a model in which the local value of $\alpha_f(\mathbf{X})$ varies linearly with the local structural mass per unit area. Specifically, we propose

$$\text{Model 1:} \quad \alpha_f(\mathbf{X}) = \alpha_{f,0}\frac{\rho_s(\mathbf{X})h(\mathbf{X})}{\rho_{s0}h_0}, \tag{33}$$

where $\rho_s(\mathbf{X})$ and $h(\mathbf{X})$ denote the density of the structure and its thickness. $\rho_{s0}h_0$ is a normalization factor, defined here to be the minimum structural mass per unit area on the structure. $\alpha_{f,0}$ is a constant that should be chosen based on $\rho_{s0}h_0$ (corresponding to the point on the structure with strongest added mass effect) in order to achieve better accuracy without losing stability.

The second model exploits the simplified model problem presented in Section 3, but with a uniform beam. For this problem, we have derived an optimal constant value of α_f, i.e. Eq. (15). Based on this finding, we propose

$$\text{Model 2:} \quad \alpha_f(\mathbf{X}) = \begin{cases} C\dfrac{M_s(\mathbf{X})M_a}{M_a - M_s(\mathbf{X})}, & \text{if } M_a > (1+\varepsilon)M_s(\mathbf{X}) \\ CM_a\varepsilon^{-1}, & \text{otherwise} \end{cases}, \tag{34}$$

where M_s and M_a represent the structural mass and the added mass of the fluid per unit area, respectively. C is a constant parameter that can be either estimated based on the region of the structure with strongest added mass effect, or calibrated to optimize accuracy. ε is a small numerical tolerance to avoid numeric overflow and division by zero. Equation (34) states that in regions where the added mass of the fluid is greater than the mass of the structure, the value of α_f reflects the ratio between these two quantities. In other regions, where the added mass effect is not significant, a large constant value of α_f is used to avoid loss of accuracy.

We define

$$M_s = \rho_s(\mathbf{X})h(\mathbf{X}) \quad \text{and} \quad M_a = \frac{\lambda\rho_f}{2\pi}, \tag{35}$$

where λ is the wavelength corresponding to the fundamental frequency of the structure (or the dominant vibration frequency of the problem). Its value can be either computed through a modal analysis or estimated based on knowledge of the problem.

5.2 | Numerical experiment

To demonstrate and compare the two models introduced above, we consider a modified Turek-Hron problem that is slightly more complex than the one introduced in Section 4. The flexible beam is designed to have four segments with various density values, instead of two segments as in Section 4. Each segment has a length of 0.0875 m. The density ρ_s is set to 300, 1,000, 2,000, and 10,000 kg/m^3 in the four segments, from left to right. Therefore, the first segment, [0, 0.0875], is the one that has the strongest added mass effect. Other parameter values involved in the problem are set to be the same as in Section 4, specifically, in Figure 11 and Table 1.

Figure 18 presents the converged solution, obtained using a 1000×200 fluid mesh, a structural mesh with 160 elements, a time step size of 2.05×10^{-4} s and 6 fluid-structure subiterations per time step. The solution is similar to the previous one in Section 4, with some subtle differences. For example, Figure 19 compares the structural displacement at three points, marked as P_1, P_2, P_3 in Figure 18. It shows that the two beams vibrate at slightly different frequencies, and point P_1 exhibits different modes.

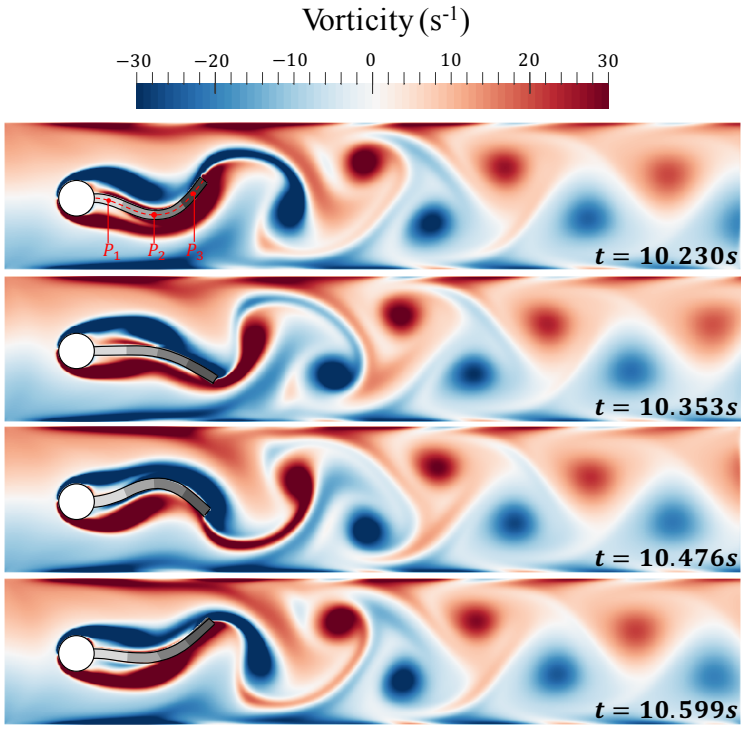

FIGURE 18 Vorticity at four time instances during one period of beam vibration.

Next, we perform three groups of numerical tests, using a 500×100 fluid mesh, a 80-element structural mesh, and with 3 fluid-structure subiterations per time step. The first group uses a constant value of α_f. We first perform a series of simulations in which the value of α_f is varied, while the time step size is set to 8.2×10^{-4} s. We found that the optimal value of α_f is 4.25, in the sense that smaller values would give less accurate solutions, while larger values would cause instability. Then, we conduct another series of simulations in which α_f is set to 4.25, while the time step size, Δt, is varied between 4.1×10^{-4} s and 1.64×10^{-3} s. The second group of tests uses a spatially varying Robin interface condition, modeled using Eq. (33), i.e. Model 1. We set $\alpha_{f,0}$ to ensure that along the first segment of the beam, $\alpha_f(\mathbf{X}) = 4.25$ (Figure 20(b)). We also vary Δt between 4.1×10^{-4} s and 1.64×10^{-3} s. The third group of tests uses a spatially varying Robin interface condition, modeled using Eq. (34), i.e. Model 2. Again, we ensure that along the first segment of the beam, $\alpha_f(\mathbf{X}) = 4.25$, and vary the time step size within the same interval.

In the third group of tests, we specify $\lambda = \bar{U}/f_v = D/St$, where $\bar{U}$ and f_v denote the mean inflow velocity and the frequency of vortex shedding, respectively. D is the diameter of the cylinder, and St is the Strouhal number. In other words, because in

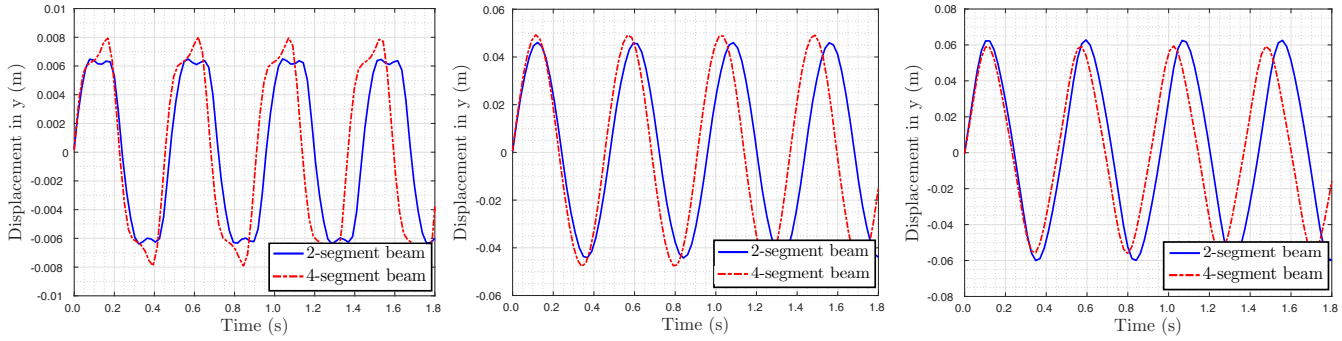

FIGURE 19 Comparison of the structural displacement in the vertical direction: (a) P_1 ($X = 0.04375$ m); (b) P_2 ($X = 0.175$ m); (c) P_3 ($X = 0.30625$ m). For each plot, time is synchronized for the ease of comparison.

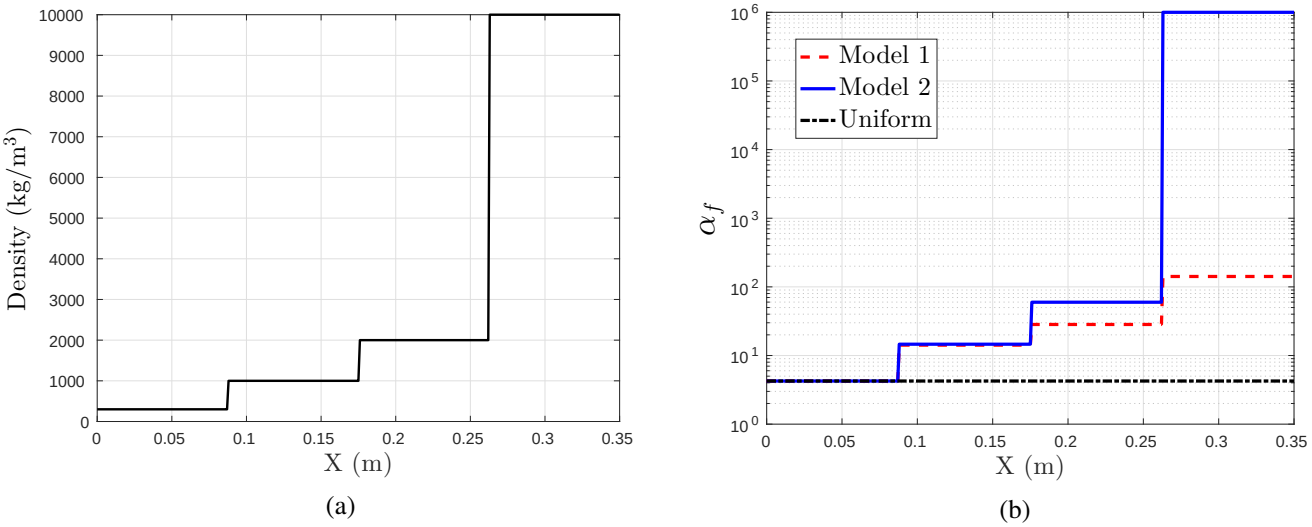

FIGURE 20 (a) Density distribution along the beam. (b) The local values of three tested α_f.

this problem the structural deformation is driven by vortex shedding, we use the frequency of vortex shedding to approximate the dominant frequency of the structure. St can be estimated based on standard measurements for flow past a fixed cylinder. For example, Williamson showed that for Reynolds number (Re) around 100, $St = 0.2175 - 5.1064/Re$ [38].

Figure 21 compares the vertical displacement of the beam's tip during one period of vibration. In addition, Table 3 presents the numerical error in the maximum vertical tip displacement. Evidently, when the time step size is fixed, both models of $\alpha_f(\mathbf{X})$ provide better accuracy than the optimal constant α_f. For example, in terms of maximum beam tip displacement, when $\Delta t = 8.2 \times 10^{-4}$ s, Model 1 reduces the error by a factor of 8.17 (2.4% vs. 19.6%), while Model 2 reduces the error by a factor of 7.54 (2.6% vs. 19.6%). Moreover, by varying the time step size, we can also observe the advantage of the spatially varying $\alpha_f(\mathbf{X})$. The solution obtained with either model of $\alpha_f(\mathbf{X})$ using $\Delta t = 1.23 \times 10^{-3}$ s is almost as accurate as the solution obtained with the optimal constant α_f using a much smaller time step, $\Delta t = 4.10 \times 10^{-4}$ s.

6 | CONCLUDING REMARKS

We have introduced a spatially varying Robin interface condition for solving fluid-structure interaction problems involving incompressible flow, non-uniform structure, and strong added mass effect. This idea is motivated both by recent findings about

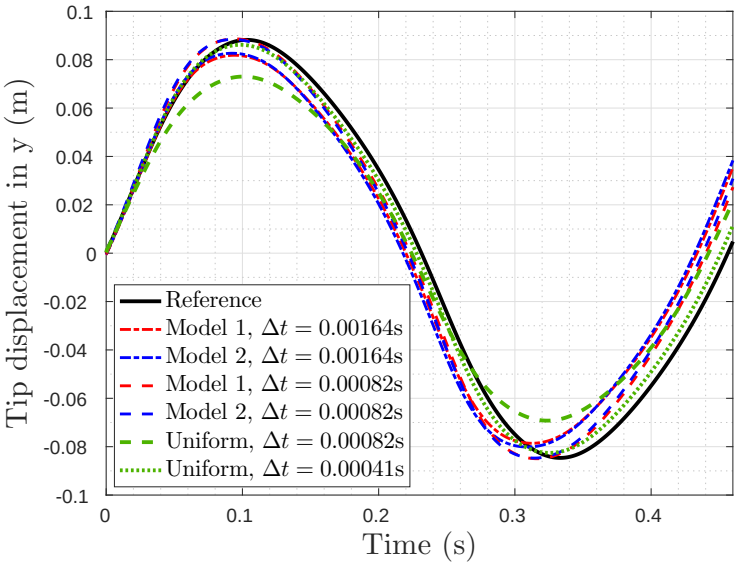

FIGURE 21 Comparison of the vertical displacement of beam tip predicted using the two modeled $\alpha_f(\mathbf{X})$ and the constant α_f. For comparison purposes, the results of one vibration cycle are presented and synchronized at the beginning of the cycle.

	Numerical error in maximum vertical tip displacement (ϵ_d)		
Time step size	Constant α_f	$\alpha_f(\mathbf{X})$ — Model 1	$\alpha_f(\mathbf{X})$ — Model 2
$\Delta t = 4.10 \times 10^{-4}$s	5.1%	1.7%	0.4%
$\Delta t = 8.20 \times 10^{-4}$s	19.6%	2.4%	2.6%
$\Delta t = 1.23 \times 10^{-3}$s	79.1%	6.2%	5.4%
$\Delta t = 1.64 \times 10^{-3}$s	96.7%	9.9%	8.9%

TABLE 3 Numerical error in the maximum vertical tip displacement obtained with the constant α_f and two modeled $\alpha_f(\mathbf{X})$.

applying a constant-parameter Robin interface condition for uniform structures, and by the practical need to efficiently simulate more complex structures with spatially varying material and geometric properties. To assess the spatially varying Robin interface condition, we have constructed and solved two model problems generalized from well-known benchmark problems, including a generalized Turek-Hron problem that exhibits large, fluid-induced structural deformation. For both model problems, we first find, as a baseline, the most accurate result that can be obtained using a constant Robin parameter for a fixed computational cost. Then, we show that a spatially varying Robin interface condition can clearly improve accuracy (by 93 times in one instance) with the same mesh resolution, time step size, and number of fluid-structure subiterations, i.e. the same computational cost. Moreover, we have presented the implementation of the spatially varying Robin interface condition using an embedded boundary method to couple a projection-based incompressible flow solver with a finite element structural dynamics solver. Furthermore, we have proposed and demonstrated two closed-form formulas to determine the spatially varying function $\alpha_f(\mathbf{X})$ based on the structure's local material and geometric properties. The first one simply conforms to the spatial variation of the structure's properties, while the second one is designed by estimating the local added mass effect and exploiting a simplified model problem. In summary, this study has provided evidence that for fluid-structure interaction problems involving non-uniform structures with spatially varying material and geometric properties, it is beneficial to apply a spatially varying Robin interface condition, as compared to the constant-parameter version recently discussed in the literature. Future studies may consider exploring additional advantages of a spatially varying Robin interface condition (e.g., reducing the number of fluid-structure subiterations), developing new formulas for the spatially varying α_f, and applying the spatially varying Robin interface condition to large-scale simulations. Also, the parameter α_f in the Robin interface condition can be generalized to temporally varying or solution-adaptive functions, which may be beneficial for certain types of problems.

ACKNOWLEDGEMENTS

The authors gratefully acknowledge the support of the National Science Foundation (NSF) under awards CBET-1751487 and CBET-1706003, and the support of the Office of Naval Research (ONR) under award N00014-19-1-2102. The authors thank Dr. Alex Main for his advice and assistance on this study.

APPENDIX A: SOLUTION OF A SIMPLIFIED MODEL PROBLEM

We employ a partitioned procedure to separate the fluid and structural sub-systems in Eqs. (11), in which the fluid and the structural governing equations are solved only once per time step. Take the solution within time step t^n to t^{n+1} as an example. Given the solution at $t = t^n$ (i.e., W^n and P^n) as the initial condition, we first solve the fluid sub-system governed by a Laplace equation with a Robin boundary condition at the fluid-structure interface, i.e.

$$\begin{cases} \nabla^2 P^{n+1} = 0 & \text{in } \Omega_f, \quad (36a) \\ \alpha_f(x)\dfrac{\partial P^{n+1}}{\partial y} + P^{n+1}b = P^n b - \alpha_f(x)\rho_f \dfrac{\partial^2 W^n}{\partial t^2} & \text{on } \Sigma, \quad (36b) \\ \dfrac{\partial P^{n+1}}{\partial y}\Big|_{\Gamma_B} = 0,\ \dfrac{\partial P^{n+1}}{\partial y}\Big|_{\Gamma_L} = \dfrac{\partial P^{n+1}}{\partial y}\Big|_{\Gamma_R},\ P^{n+1}\Big|_{\Gamma_L} = P^{n+1}\Big|_{\Gamma_R}. & (36c) \end{cases}$$

Then, the resulting pressure load on Σ at $t = t^{n+1}$ (i.e., $P^{n+1}|_\Sigma$) is transferred to structural sub-system. Next, the structural solution is advanced from t^n to t^{n+1} by solving:

$$\begin{cases} EI\dfrac{\partial^4 W}{\partial x^4} + \rho_s bh\dfrac{\partial^2 W}{\partial t^2} = P^{n+1}|_\Sigma b \qquad \text{in } (t^n, t^{n+1}) \times \Omega_s, & (37a) \\ W(x, t^n) = W^n, & (37b) \\ \dfrac{\partial W(x, t^n)}{\partial t} = \dfrac{\partial W^n}{\partial t}, & (37c) \\ W\Big|_{\partial\Omega_s} = 0,\ \dfrac{\partial^2 W}{\partial x^2}\Big|_{\partial\Omega_s} = 0. & (37d) \end{cases}$$

More specifically, Eqs. (36) are solved using the conventional two-dimensional five-point finite difference scheme. Eqs. (37) are first semi-discretized using a standard Galerkin finite-element method. The resulting semi-discrete equation of motion can be written as

$$\mathbf{M}\ddot{W}_h + \mathbf{K}W_h = \mathbf{f}_{ext}, \quad (38)$$

where the subscript "h" denotes the semi-discrete solution, $\mathbf{M}$ is the mass matrix, $\mathbf{K}$ is the stiffness matrix and $\mathbf{f}_{ext}$ is the vector of external dynamic loads. Eq. (38) is integrated in time using the Hilber-Hughes-Taylor α (HHT-α) method, which yields a linear system for solution at $t = t^{n+1}$ (i.e., W_h^{n+1}):

$$\left[\bar{\mathbf{K}}\right] W_h^{n+1} = \left[\bar{\mathbf{F}}\right], \quad (39)$$

where

$$\left[\bar{\mathbf{K}}\right] = \frac{\mathbf{M}}{\beta\Delta t^2} + (1-\alpha)\mathbf{K}, \quad (40)$$

$$\left[\bar{\mathbf{F}}\right] = (1-\alpha)\mathbf{f}_{ext}^{n+1} + \alpha\mathbf{f}_{ext}^{n} + \left(\frac{\mathbf{M}}{\beta\Delta t^2} - \alpha\mathbf{K}\right) W_h^n + \frac{\mathbf{M}}{\beta\Delta t}\dot{W}_h^n + \mathbf{M}\left(\frac{1}{2\beta} - 1\right)\ddot{W}_h^n. \quad (41)$$

Then, the acceleration and velocity of the beam at $t = t^{n+1}$ are computed by

$$\ddot{W}_h^{n+1} = \frac{1}{\beta\Delta t^2}\left[W_h^{n+1} - W_h^n - \Delta t\dot{W}_h^n\right] - \left(\frac{1}{2\beta} - 1\right)\ddot{W}_h^n, \quad (42)$$

$$\dot{W}_h^{n+1} = \dot{W}_h^n + \Delta t\left[(1-\gamma)\ddot{W}_h^n + \gamma\ddot{W}_h^{n+1}\right]. \quad (43)$$

The values of α, β and γ in the equations above are set by

$$\begin{aligned}\alpha &= 1/3,\\ \beta &= (1+\alpha)^2/4,\\ \gamma &= 1/2+\alpha,\end{aligned}$$

which makes the scheme unconditionally stable.

Remark: We also solve the same model problem using a monolithic procedure, primarily as a way to verify the implementation of the above partitioned procedure. In the monolithic procedure, Eqs. (11a) and (11c) are discretized in space and time, yielding a system of linear equations that couples the beam displacement and fluid pressure. Specificially,

$$\begin{cases} EI\dfrac{W_{i-2}^{n+1}-4W_{i-1}^{n+1}+6W_i^{n+1}-4W_{i+1}^{n+1}+W_{i+2}^{n+1}}{\Delta x^4}+\rho_{s,i}bh\dfrac{W_i^{n+1}-2W_i^n+W_i^{n-1}}{\Delta t^2}=P_i^{n+1}b, & \text{(44a)}\\ P_{i+1,j}^{n+1}+P_{i-1,j}^{n+1}+P_{i,j+1}^{n+1}+P_{i,j-1}^{n+1}-4P_{i,j}^{n+1}=0. & \text{(44b)}\end{cases}$$

Figure 22 compares the solutions obtained using the partitioned and monolithic procedures for Case 1. The fluid and structural meshes and the time step size are kept the same. As expected, the two numerical solutions are in close agreement.

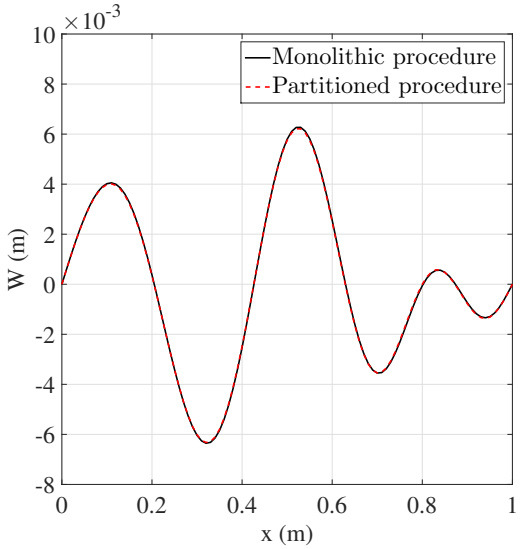

FIGURE 22 Comparison of the solutions of the partitioned and monolithic procedures for Case 1: Beam displacement at $t = 10^{-4}$ s.

References

[1] Piperno S, Farhat C, Larrouturou B. Partitioned procedures for the transient solution of coupled aroelastic problems Part I: Model problem, theory and two-dimensional application. *Computer methods in applied mechanics and engineering* 1995; 124(1-2): 79–112.

[2] Felippa CA, Park K, Farhat C. Partitioned analysis of coupled mechanical systems. *Computer methods in applied mechanics and engineering* 2001; 190(24-25): 3247–3270.

[3] Guidoboni G, Glowinski R, Cavallini N, Canic S. Stable loosely-coupled-type algorithm for fluid–structure interaction in blood flow. *Journal of Computational Physics* 2009; 228(18): 6916–6937.

[4] Farhat C, Rallu A, Wang KG, Belytschko T. Robust and provably second-order explicit–explicit and implicit–explicit staggered time-integrators for highly non-linear compressible fluid–structure interaction problems. *International Journal for Numerical Methods in Engineering* 2010; 84(1): 73–107.

[5] Nobile F, Pozzoli M, Vergara C. Time accurate partitioned algorithms for the solution of fluid–structure interaction problems in haemodynamics. *Computers & Fluids* 2013; 86: 470–482.

[6] Stein K, Benney R, Kalro V, Tezduyar TE, Leonard J, Accorsi M. Parachute fluid–structure interactions: 3-D Computation. *Computer Methods in Applied Mechanics and Engineering* 2000; 190(3-4): 373–386.

[7] Farhat C, Wang KG, Main A, et al. Dynamic implosion of underwater cylindrical shells: experiments and computations. *International Journal of Solids and Structures* 2013; 50(19): 2943–2961.

[8] Wang KG, Lea P, Farhat C. A computational framework for the simulation of high-speed multi-material fluid–structure interaction problems with dynamic fracture. *International Journal for Numerical Methods in Engineering* 2015; 104(7): 585–623.

[9] Chung H, Cao S, Philen M, Beran PS, Wang KG. CFD-CSD coupled analysis of underwater propulsion using a biomimetic fin-and-joint system. *Computers & Fluids* 2018.

[10] Cao S, Zhang Y, Liao D, Zhong P, Wang KG. Shock-Induced Damage and Dynamic Fracture in Cylindrical Bodies Submerged in Liquid. *International Journal of Solids and Structures* 2019.

[11] Liu G, Geng B, Zheng X, Xue Q, Dong H, Lauder GV. An image-guided computational approach to inversely determine in vivo material properties and model flow-structure interactions of fish fins. *Journal of Computational Physics* 2019.

[12] Causin P, Gerbeau JF, Nobile F. Added-mass effect in the design of partitioned algorithms for fluid–structure problems. *Computer methods in applied mechanics and engineering* 2005; 194(42): 4506–4527.

[13] Förster C, Wall WA, Ramm E. Artificial added mass instabilities in sequential staggered coupling of nonlinear structures and incompressible viscous flows. *Computer methods in applied mechanics and engineering* 2007; 196(7): 1278–1293.

[14] Gerbeau JF, Vidrascu M. A quasi-Newton algorithm based on a reduced model for fluid-structure interaction problems in blood flows. *ESAIM: Mathematical Modelling and Numerical Analysis* 2003; 37(4): 631–647.

[15] Deparis S, Fernández MA, Formaggia L. Acceleration of a fixed point algorithm for fluid-structure interaction using transpiration conditions. *ESAIM: Mathematical Modelling and Numerical Analysis* 2003; 37(4): 601–616.

[16] Badia S, Quaini A, Quarteroni A. Modular vs. non-modular preconditioners for fluid–structure systems with large added-mass effect. *Computer Methods in Applied Mechanics and Engineering* 2008; 197(49-50): 4216–4232.

[17] Radtke L, Larena-Avellaneda A, Debus ES, Düster A. Convergence acceleration for partitioned simulations of the fluid-structure interaction in arteries. *Computational Mechanics* 2016; 57(6): 901–920.

[18] Badia S, Nobile F, Vergara C. Fluid–structure partitioned procedures based on Robin transmission conditions. *Journal of Computational Physics* 2008; 227(14): 7027–7051.

[19] Nobile F, Vergara C. Partitioned algorithms for fluid-structure interaction problems in haemodynamics. *Milan journal of mathematics* 2012; 80(2): 443–467.

[20] Nobile F, Pozzoli M, Vergara C. Inexact accurate partitioned algorithms for fluid–structure interaction problems with finite elasticity in haemodynamics. *Journal of Computational Physics* 2014; 273: 598–617.

[21] Fernández MA, Mullaert J, Vidrascu M. Explicit Robin–Neumann schemes for the coupling of incompressible fluids with thin-walled structures. *Computer Methods in Applied Mechanics and Engineering* 2013; 267: 566–593.

[22] Fernández MA, Landajuela M, Vidrascu M. Fully decoupled time-marching schemes for incompressible fluid/thin-walled structure interaction. *Journal of Computational Physics* 2015; 297: 156–181.

[23] Cao S, Main A, Wang KG. Robin-Neumann transmission conditions for fluid-structure coupling: Embedded boundary implementation and parameter analysis. *International Journal for Numerical Methods in Engineering* 2018; 115(5): 578–603.

[24] Li L, Henshaw W, Banks J, Schwendeman D, Main A. A stable partitioned FSI algorithm for incompressible flow and deforming beams. *Journal of Computational Physics* 2016; 312: 272–306.

[25] Basting S, Quaini A, Čanić S, Glowinski R. Extended ALE Method for fluid–structure interaction problems with large structural displacements. *Journal of Computational Physics* 2017; 331: 312–336.

[26] Gerardo-Giorda L, Nobile F, Vergara C. Analysis and optimization of Robin–Robin partitioned procedures in fluid-structure interaction problems. *SIAM Journal on Numerical Analysis* 2010; 48(6): 2091–2116.

[27] Nie S, Cao Y, Wu Z. Numerical simulation of parafoil inflation via a Robin–Neumann transmission-based approach. *Proceedings of the Institution of Mechanical Engineers, Part G: Journal of Aerospace Engineering* 2018; 232(4): 797–810.

[28] Errera MP, Chemin S. Optimal solutions of numerical interface conditions in fluid–structure thermal analysis. *Journal of Computational Physics* 2013; 245: 431–455.

[29] Yu Y, Bargos FF, You H, Parks ML, Bittencourt ML, Karniadakis GE. A partitioned coupling framework for peridynamics and classical theory: Analysis and simulations. *Computer Methods in Applied Mechanics and Engineering* 2018; 340: 905–931.

[30] Banks JW, Henshaw WD, Schwendeman DW. An analysis of a new stable partitioned algorithm for FSI problems. Part II: Incompressible flow and structural shells. *Journal of Computational Physics* 2014; 268: 399–416.

[31] Turek S, Hron J. Proposal for numerical benchmarking of fluid-structure interaction between an elastic object and laminar incompressible flow. In: Springer. 2006 (pp. 371–385).

[32] Griffith BE, Peskin CS. On the order of accuracy of the immersed boundary method: Higher order convergence rates for sufficiently smooth problems. *Journal of Computational Physics* 2005; 208(1): 75–105.

[33] Tseng YH, Ferziger JH. A ghost-cell immersed boundary method for flow in complex geometry. *Journal of computational physics* 2003; 192(2): 593–623.

[34] Jomaa Z, Macaskill C. Numerical solution of the 2D Poisson equation on an irregular domain with Robin boundary conditions. *ANZIAM Journal* 2008; 50: 413–428.

[35] Jomaa Z, Macaskill C. The Shortley–Weller embedded finite-difference method for the 3D Poisson equation with mixed boundary conditions. *Journal of Computational Physics* 2010; 229(10): 3675–3690.

[36] Belytschko T, Liu WK, Moran B, Elkhodary K. *Nonlinear finite elements for continua and structures*. John wiley & sons . 2013.

[37] Main A. A study of fluid-structure interaction on overlapping grids with a focus on flexible beams. tech. rep., Technical Report LLNL-TR-643858, Lawrence Livermore National Laboratory; Livermore, CA (United States): 2013.

[38] Williamson CH. Oblique and parallel modes of vortex shedding in the wake of a circular cylinder at low Reynolds numbers. *Journal of Fluid Mechanics* 1989; 206: 579–627.